



**MACQUARIE**  
University  
SYDNEY · AUSTRALIA

Department of Earth and Environmental Sciences

Macquarie University, NSW 2109, Australia

Phone +61 (0)4 77300674

Email [maria-constanza.manassero@mq.edu.au](mailto:maria-constanza.manassero@mq.edu.au)

November 15<sup>th</sup>, 2022

We present an original manuscript entitled “ Joint probabilistic inversion of 3D magnetotelluric and seismic data: Lithospheric structure and melting dynamics in southeast Australia” by M.C. Manassero<sup>1</sup>, S. Özaydin<sup>1</sup>, J. C. Afonso<sup>1,2</sup>, J. Shea<sup>1,3</sup>, S. Thiel<sup>4,5</sup>, A. Kirkby<sup>6</sup>, I. Fomin<sup>1</sup> and K. Czarnota<sup>7</sup>.

This paper is a non-peer reviewed preprint submitted to EarthArXiv. The preprint is going to be submitted for peer review to Journal of Geophysical Research: Solid Earth on 22<sup>th</sup> November, 2022.

Yours Sincerely,

Maria Constanza Manassero\* ([maria-constanza.manassero@mq.edu.au](mailto:maria-constanza.manassero@mq.edu.au))

Sinan Özaydin ([sinan.ozaydin@mq.edu.au](mailto:sinan.ozaydin@mq.edu.au))

Juan Carlos Afonso ([juan.afonso@mq.edu.au](mailto:juan.afonso@mq.edu.au))

Joshua Shea ([Joshua.shea1@hdr.mq.edu.au](mailto:Joshua.shea1@hdr.mq.edu.au))

Stephan Thiel ([Stephan.Thiel@sa.gov.au](mailto:Stephan.Thiel@sa.gov.au))

Alison Kirkby ([alkirkby@gmail.com](mailto:alkirkby@gmail.com))

Ilya Fomin ([ilya.fomin@mq.edu.au](mailto:ilya.fomin@mq.edu.au))

and Karol Czarnota.

<sup>1</sup> Australian Research Council Centre of Excellence for Core to Crust Fluid Systems/GEMOC, Department of Earth and Environmental Sciences, Macquarie University.

<sup>2</sup> Department of Applied Earth Sciences, University of Twente, The Netherlands

<sup>3</sup> Department of Materials, The University of Manchester, Manchester M13 9PL, United Kingdom

<sup>4</sup> Department of Earth Sciences, University of Adelaide, Adelaide, SA 5005, Australia

<sup>5</sup> Geological Survey of South Australia, Adelaide, SA 5001, Australia

<sup>6</sup> GNS Science, Wairakei Research Centre, Taupo, New Zealand

<sup>7</sup> Geoscience Australia, Canberra, ACT, 2601, Australia.

\*Corresponding author

Australian Research Council Centre of Excellence for Core to Crust Fluid System (CCFS)

Department of Earth and Environmental Sciences, Macquarie University, Sydney, NSW 2109, Australia

email: [maria-constanza.manassero@mq.edu.au](mailto:maria-constanza.manassero@mq.edu.au)

1 **Joint probabilistic inversion of 3D magnetotelluric and**  
2 **seismic data: Lithospheric structure and melting**  
3 **dynamics in southeast Australia**

4 **M.C. Manassero<sup>1</sup>, S. Özaydın<sup>1</sup>, J.C. Afonso<sup>1,2</sup>, J. Shea<sup>1,3</sup>, S. Thiel<sup>4,5</sup>, A.**  
5 **Kirkby<sup>6</sup>, I. Fomin<sup>1</sup> and K. Czarnota<sup>7</sup>**

6 <sup>1</sup>Australian Research Council Centre of Excellence for Core to Crust Fluid Systems/GEMOC, School of  
7 Natural Sciences, Macquarie University, Sydney, Australia.

8 <sup>2</sup>Department of Applied Earth Sciences, University of Twente, The Netherlands

9 <sup>3</sup>Department of Materials, The University of Manchester, Manchester M13 9PL, United Kingdom

10 <sup>4</sup>Department of Earth Sciences, University of Adelaide, Adelaide, SA 5005, Australia

11 <sup>5</sup>Geological Survey of South Australia, Adelaide, SA 5001, Australia

12 <sup>6</sup>GNS Science, Wairakei Research Centre, Taupo, New Zealand.

13 <sup>7</sup>Geoscience Australia, Canberra, ACT, 2601, Australia.

14 **Key Points:**

- 15 • We apply a novel approach for joint probabilistic inversions of 3D magnetotelluric  
16 and seismic data.  
17 • We use the new method to image the lithosphere-asthenosphere system beneath  
18 southeastern of Australia.  
19 • The imaged lithosphere correlates with the location of volcanic centers and pro-  
20 vides insights on the melt production in the region.

---

Corresponding author: Maria Constanza Manassero, [maria-constanza.manassero@mq.edu.au](mailto:maria-constanza.manassero@mq.edu.au)



## 21 Abstract

22 The thermochemical structure of the lithosphere exerts control on melting mech-  
23 anisms in the mantle as well as the location of volcanic eruptions and ore deposits. Imag-  
24 ing the complex interactions between the lithosphere and asthenospheric mantle require  
25 the joint inversion of multiple data sets and their uncertainties. In particular, the com-  
26 bination of temperature and electrical conductivity with data proxies for bulk composi-  
27 tion and elusive minor phases is a crucial step towards fully understanding large-scale  
28 lithospheric structure and melting. We apply a novel probabilistic approach for joint in-  
29 versions of 3D magnetotelluric and seismic data to image the lithosphere beneath south-  
30 east Australia. Results show a highly heterogeneous lithospheric structure that corre-  
31 lates with the location of Cenozoic volcanism and deep conductivity anomalies. In re-  
32 gions where the conductivities have been at odds with sub-lithospheric temperatures and  
33 seismic velocities, we observe that the joint inversion provides conductivity values con-  
34 sistent with other observations. The results reveal a strong relationship between meta-  
35 somatized regions in the mantle and i) the limits of geological provinces in the crust, which  
36 elucidates the subduction-accretion process in the region; ii) distribution of leucitite and  
37 basaltic magmatism; iii) independent geochemical data, and iv) a series of lithospheric  
38 steps which constitute areas prone to generating small-scale instabilities in the astheno-  
39 sphere. This scenario suggests that shear-driven upwelling and edge-driven convection  
40 are the dominant melting mechanisms in eastern Australia rather than mantle plume ac-  
41 tivity, as conventionally conceived. Our study offers an integrated lithospheric model for  
42 southeastern Australia and provides insights into the feedback mechanism driving sur-  
43 face processes.

## 44 Plain Language Summary

45 The lithosphere is the outermost rigid layer of the Earth and the focus of impor-  
46 tant geological processes such as earthquakes (seismic activity), volcanism, and miner-  
47 alization. The location of these seismically active zones, magma intrusion/production,  
48 and ore deposits often coincide with deep discontinuities in the lithospheric structure.  
49 Imaging the structure of the lithosphere using geophysical techniques is then crucial to  
50 fully understand the nature of these processes. Obtaining the most reliable images of the  
51 lithospheric structure requires the joint analysis of two or more geophysical data sets.  
52 In particular, the combination of magnetotellurics (an electromagnetic technique) and  
53 seismic data holds great potential due to their complementary sensitivity to the Earth's  
54 properties. Combining a joint analysis with a probabilistic approach help us understand  
55 the variability of the lithospheric structure better since they provide a large number of  
56 models that can explain the data. Given the good data coverage in southeast Australia,  
57 we use a new probabilistic approach for the joint analysis of magnetotelluric and seis-  
58 mic data to image the lithosphere structure beneath this region. Our results show a com-  
59 plex lithospheric structure in line with the location of volcanic centers and the tectonic  
60 history of the region. Lithospheric composition derived from the models also provides  
61 significant insights into how melt production in the area might have occurred.

## 62 1 Introduction

63 Magnetotellurics (MT) has great potential for investigating metasomatism and tectono-  
64 magmatic evolution in the lithosphere (e.g., Wannamaker et al., 2008; Comeau et al., 2015;  
65 Aivazpourporgou et al., 2015; Wannamaker et al., 2014; Bedrosian, 2016; Blatter et al.,  
66 2022; Özyaydın & Selway, 2022; Cordell et al., 2022). Imaging the deep thermochemical  
67 structure of the lithosphere is crucial due to its connection with surface expressions of  
68 fluid and melt pathways, such as the location of ore deposits (e.g., Griffin et al., 2013;  
69 Heinson et al., 2018; Kirkby et al., 2022) and volcanic centers (Davies et al., 2015). One  
70 of the main limitations of the MT method lies, however, in constraining deep conduc-

71 tivity structures, particularly beneath shallow conductive features. This is due to the  
 72 the diffusive behaviour of electromagnetic waves and the high sensitivity of MT to con-  
 73 ductors (Jones, 1999). The MT method is also ambiguous in discerning the different fac-  
 74 tors that affect electrical conductivity, such as temperature, water/melt content and com-  
 75 position. Unlocking the full potential of the MT method requires the development of method-  
 76 ologies that can assign meaningful physical interpretations to conductivity anomalies and  
 77 discriminate between their causes (Selway, 2014).

78 A widely adopted methodology to reduce feature ambiguity is combining MT with  
 79 other geophysical data sets via joint inversions (e.g. Khan et al., 2006; Gallardo & Meju,  
 80 2007; Jegen et al., 2009; Moorkamp et al., 2010; Afonso, Rawlinson, et al., 2016; Jones  
 81 et al., 2017). By exploiting the complementary sensitivities of different data sets to the  
 82 properties of interest, joint inversions minimize the range of acceptable models consist-  
 83 ent with the available data and increase model resolution (cf. Moorkamp et al., 2007;  
 84 Afonso et al., 2013a; Afonso, Rawlinson, et al., 2016; Afonso, Moorkamp, & Fullea, 2016).  
 85 For example, in the case of MT and seismic data, both data sets are sensitive (to dif-  
 86 ferent degrees) to the background thermal and compositional structure of the lithosphere.  
 87 However, only MT is strongly sensitive to minor conductive phases (e.g., hydrous min-  
 88 erals and graphite), hydrogen content or small-scale melt/fluid pathways (Karato, 1990,  
 89 2006; Evans, 2012; Yoshino, 2010; Khan, 2016; Selway, 2014; Manassero et al., 2021). In  
 90 this way, joint MT+seismic inversions hold great potential for improving the resolution  
 91 of conductivity structures (e.g., Moorkamp et al., 2007, 2010; Gallardo & Meju, 2007;  
 92 Afonso, Moorkamp, & Fullea, 2016), detecting the presence of partial melt (cf., Selway  
 93 & O’Donnell, 2019; Evans et al., 2019) and fluid pathways (cf., García-Yeguas et al., 2017;  
 94 Bennington et al., 2015) in the lithosphere, and understanding the relationship of these  
 95 lithospheric features with the location of ore deposits (e.g., Takam Takougang et al., 2015)  
 96 and metasomatized lithologies (e.g., Snyder et al., 2014).

97 In addition to the benefits of joint inversions, valuable information about model  
 98 uncertainties (Tarantola, 2005; Afonso, Rawlinson, et al., 2016; Manassero et al., 2021)  
 99 can be obtained via probabilistic approaches. These approaches provide a range of mod-  
 100 els and their probability in explaining the observations by sampling millions of possible  
 101 models and computing a forward solution for each of them. Thus, probabilistic inver-  
 102 sions naturally address the non-uniqueness problem in geophysics (particularly in MT)  
 103 and quantify model ambiguity (Tarantola, 2005; Gregory, 2005; Rosas-Carbajal et al.,  
 104 2013). Given their intrinsic computational cost, simulation-based probabilistic approaches  
 105 are limited to problems where fast forward operators are available. In the case of 3D MT  
 106 inversions, fully probabilistic methods have been infeasible due to the large CPU time  
 107 required by the associated forward problem (Miensopust et al., 2013). In order to ad-  
 108 dress this limitation, Manassero et al. (2020) developed a novel strategy, referred to as  
 109 RB+MCMC, that allows obtaining fast and accurate approximations of the forward so-  
 110 lution and performing joint probabilistic inversions of 3D MT data with other data sets  
 111 (Manassero et al., 2021). Potential applications and the efficiency of the method to solve  
 112 the joint inverse problem of MT and seismic data were previously demonstrated with whole-  
 113 lithosphere synthetic examples in our previous paper (Manassero et al., 2021).

114 In this work, we apply the new method to the dense MT and seismic data sets in  
 115 south-eastern Australia to provide new constraints on its complex lithospheric structure.  
 116 This region has undergone several episodes of accretion-subduction and extension pro-  
 117 cesses (Glen, 2005), lithospheric deformation (Moresi et al., 2014) and contains part of  
 118 the mafic Eastern Australian Volcanic Province (EAVP), one of the most voluminous  
 119 intraplate volcanic regions in the world (Johnson et al., 1989; Sutherland et al., 2012).  
 120 The EAVP is somewhat unique since half its volcanism is age-progressive and commonly  
 121 linked to a hot mantle plume (e.g., Sutherland et al., 2012; Davies et al., 2015), whereas  
 122 the remaining half is not age-progressive with no obvious melting mechanism (Wellman  
 123 & McDougall, 1974). To further exacerbate this issue, lava compositions throughout the

124 EAVP (including both age-progressive and non-age-progressive volcanic centers) argue  
 125 for low-temperature melting of metasomatized mantle source lithologies. In contradic-  
 126 tion to the presence of a hot mantle plume, these compositions suggest a source driven  
 127 by mild perturbations in mantle temperatures (Shea et al., 2022), such as shear-driven  
 128 upwelling and edge-driven convection (Davies & Rawlinson, 2014; Demidjuk et al., 2007).  
 129 Since thermo-physical variations in the lithosphere exert control on melt composition and  
 130 eruption locations (Davies et al., 2015), reliable models of the lithospheric first-order struc-  
 131 ture are necessary to explain these controversies.

132 Independent results from conventional ambient noise and teleseismic tomography  
 133 (Rawlinson et al., 2016; Davies et al., 2015; Young et al., 2013), xenolith thermobarom-  
 134 etry (e.g., Lu et al., 2018), thermal modeling (e.g., Tesauro et al., 2020) and a recent 3D  
 135 conductivity model (Kirkby et al., 2020) have yielded important information about the  
 136 lithospheric structure beneath southeast Australia. However, some discrepancies are ob-  
 137 served between these models despite the fact that they all describe the same region. Be-  
 138 neath the Eastern Volcanics, for example, the sub-lithospheric mantle conductivities in  
 139 the model of Kirkby et al. (2020) are at odds with the mantle temperatures inferred by  
 140 Tesauro et al. (2020) and the low velocities imaged by Rawlinson et al. (2016) and Davies  
 141 et al. (2015). In this work, we attempt to bridge the results of independent studies and  
 142 obtain reliable lithospheric models that are compatible with independent geophysical,  
 143 geological, and geochemical evidence in south-eastern Australia. In particular, we aim  
 144 to assess how the lithospheric structure may have influenced melting mechanisms for the  
 145 EAVP and to better understand overall melting dynamics in intraplate settings.

146 To achieve these goals, we use our probabilistic approach to obtain thermal, seis-  
 147 mic velocity, and electrical conductivity models (with their uncertainties) by jointly in-  
 148 verting 3D magnetotelluric data and seismic velocities from a tomographic model (Rawl-  
 149 inson et al., 2016). Bulk water content maps are derived from the inversion results to  
 150 further understand the connection between geodynamic processes and metasomatism.

## 151 2 Geological background

152 The Tasmanides in eastern Australia are a complex orogenic system that developed  
 153 from west to east through repetitive cycles of subduction and accretion along the east-  
 154 ern margin of Gondwana (Glen, 2005, 2013; Champion et al., 2016; Rosenbaum, 2018).  
 155 This region is broadly divided into the Delamerian Orogen in the west (early-Palaeozoic)  
 156 and the younger (mid-Paleozoic) Lachlan Orogen in the southeast (Figure 1.a). Much  
 157 of the geological complexity in the area can be explained by a geodynamic model of a  
 158 micro-continent collision and later development of an orocline, referred to as the Lach-  
 159 lan Orocline model (Cayley, 2011; Cayley & Musgrave, 2015; Moresi et al., 2014; Mus-  
 160 grave, 2015). The major structures described in this model are curved crustal geome-  
 161 tries with an eastward rotation that persists below the base of the crust (Musgrave, 2015),  
 162 which have been imaged by gravity, magnetic, and potential field data (e.g., Musgrave  
 163 & Rawlinson, 2010; Nakamura & Milligan, 2015; Nakamura, 2016, see Figure 1.c-d.); am-  
 164 bient noise tomography in the crust (e.g., Young et al., 2013; Pilia et al., 2015, see Fig-  
 165 ure 10.d); 2D MT conductivity models (Aivazpourporgou et al., 2015) and a recent 3D  
 166 MT conductivity model (Kirkby et al., 2020; Heinson et al., 2021). This latter 3D con-  
 167 ductivity model shows, for the first time, that some of those crustal structures persist  
 168 below the Moho, providing new insights about the lithospheric architecture and geody-  
 169 namic history of the region.

170 Throughout the late Mesozoic and the entire Cenozoic, eastern Australia has been  
 171 consistently subjected to voluminous mafic intraplate volcanism, which formed the ex-  
 172 tensive Eastern Australian Volcanic Province (EAVP, Johnson et al., 1989; Sutherland  
 173 et al., 2012; Shea et al., 2022). Several regions throughout northern and south-eastern  
 174 Australia contain recent eruptions; in northern Australia, the Kinrara vent contains lavas

175  $\sim 7 \text{ ka} \pm 2 \text{ ka}$  (Cohen et al., 2017), while the Mount Gambier, Newer Volcanics (NV) con-  
 176 tains lavas  $\sim 4\text{--}7.5 \text{ ka}$  (Blackburn et al., 1982; Smith & Prescott, 1987).

177 The EAVP comprises 67 separate volcanic centers with two dominant volcanic center  
 178 compositions: basalt and potassic leucitite (Figure 1.b). While basaltic volcanics erupted  
 179 through thinner lithosphere ( $< 110 \text{ km}$ ) along the eastern and south-eastern seaboard,  
 180 the leucitite volcanic centers lie on thick lithosphere ( $> 125 \text{ km}$ ) in central New South  
 181 Wales and central Victoria (Davies & Rawlinson, 2014; Rawlinson et al., 2017). This leuci-  
 182 tite suite represents the most petrologically atypical and extraordinarily enriched melt  
 183 compositions reported for mafic melts in eastern Australia (Cundari, 1973; Birch, 1978).  
 184 Particularly, they represent melts from the most pervasively metasomatized source as-  
 185 semblages, likely a Ti-bearing oxide phlogopite websterite  $\pm$  apatite (Shea et al., 2022),  
 186 which deviate from anhydrous peridotites. A review of the intra-continental volcanic cen-  
 187 ters in the EAVP and their source assemblages is presented in Shea et al. (2022). The  
 188 lack of anhydrous peridotite and the abundance of hydrous minerals in their mantle source  
 189 assemblages is of particular importance to this work, indicating widespread mantle meta-  
 190 somatism beneath eastern Australia.

### 191 3 Methods and data sets

#### 192 3.1 Data

193 The data used in our joint probabilistic inversion include magnetotelluric (MT) data  
 194 from the AusLAMP array (Australian Lithospheric Architecture Magnetotelluric Project)  
 195 in southeast Australia and the P-wave velocity model of Rawlinson et al. (2016) as seis-  
 196 mic data. The long-period MT data were acquired at 298 AusLAMP stations (blue tri-  
 197 angles in Figure 1.f) across a  $\sim 55 \text{ km}$  spaced array covering an area of  $950 \times 950 \text{ km}$ .  
 198 Details about the data acquisition and processing are given in Kirkby et al. (2020). The  
 199 MT data are the full impedance tensor for periods between 6.4 to 40,000s. Error floors  
 200 are set to 5% of  $\max(|Z_{xx}|, |Z_{xy}|)$  for the components  $Z_{xx}$  and  $Z_{xy}$  and 5% of  $\max(|Z_{yy}|, |Z_{yx}|)$   
 201 for the components  $Z_{yy}$  and  $Z_{yx}$ . We assume uncorrelated data errors that follow a dou-  
 202 ble exponential distribution (e.g., Farquharson & Oldenburg (1998); Rosas-Carbajal et  
 203 al. (2013); Manassero et al. (2021)).

204 The P-wave velocity model used in this study (Rawlinson et al., 2016) was constructed  
 205 from teleseismic tomography using data from the mainland component of the WOMBAT  
 206 transportable seismic array (Rawlinson et al., 2015). In order to account for the unre-  
 207 solved crustal component of the teleseismic arrival time residuals, the model includes a  
 208 detailed crustal model from ambient noise tomography (Young et al., 2013) and the Moho  
 209 from AuSREM (Kennett & Salmon, 2012) in the starting model. Using this model, we  
 210 obtain seismic velocities on a data-point grid of  $50 \times 50 \text{ km}$  at the surface (shown in red  
 211 dots in Figure 1.f) and 24 points between the surface and 340 km depth. The data er-  
 212 rors are assumed to be uncorrelated and normally distributed with a standard deviation  
 213 of 1% of the velocity. Examples of data and data fits for MT data and seismic veloci-  
 214 ties are shown in Figures 2 and 3, respectively. Additional figures can be found in the  
 215 Supplementary Material.

#### 216 3.2 Bayesian inversion and model parameterization

217 In the Bayesian or probabilistic approach to the inverse problem, inference about  
 218 the model parameters  $\mathbf{m}$ , given observed data  $\mathbf{d}$ , is based on the so-called posterior prob-  
 219 ability density function (PDF):

$$P(\mathbf{m}|\mathbf{d}) = \frac{P(\mathbf{d}|\mathbf{m})P(\mathbf{m})}{P(\mathbf{d})} \propto \mathcal{L}(\mathbf{m})P(\mathbf{m}) \propto \exp(\phi)P(\mathbf{m}), \quad (1)$$



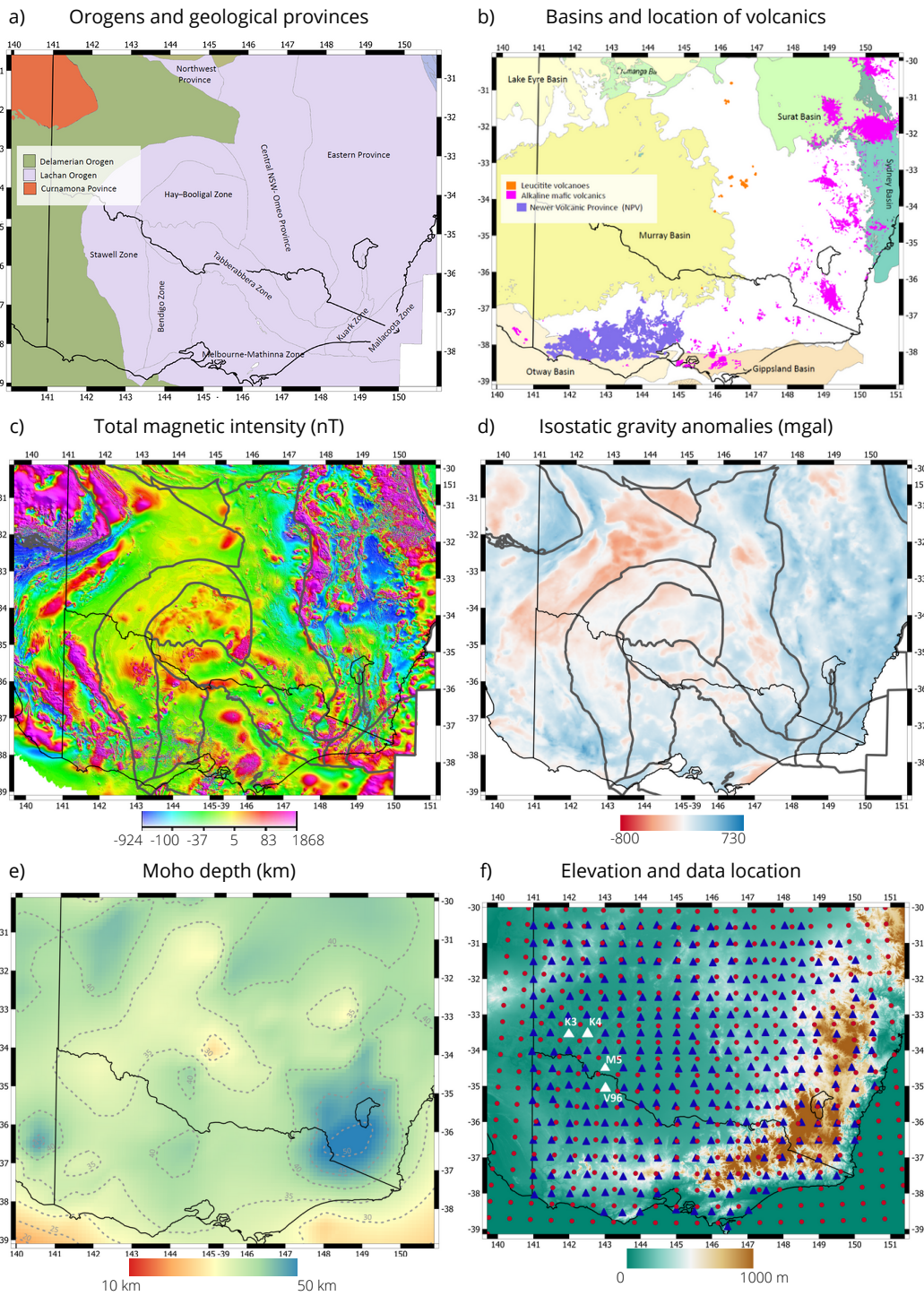


**Figure 1.** Maps showing (a) orogens that comprise the Tasmanides of southeastern Australia with grey outline denoting geological provinces (Raymond et al., 2018); (b) Mesozoic to Cenozoic sedimentary basins after Raymond et al. (2012), leucitites volcanoes (orange) and basaltic volcanics (pink) after Shea et al. (2022). The basaltic in NV are highlighted in purple. (c) Total magnetic intensity map (TMI) which includes airborne-derived TMI data for onshore and near-offshore continental areas (Nakamura & Milligan, 2015). (d) Isostatic residual anomaly map (Nakamura, 2016). (e) Moho depth from the AusREM model (Kennett & Salmon, 2012) where 5km-contour lines are shown in dashed-grey. (f) Elevation map of southeast Australia including the AusLAMP MT stations (blue triangles) and the location of the velocity data (red dots). Panel (c) and (d) show major tectonic boundaries are outlined in grey. White triangles indicate stations where data fits are shown.

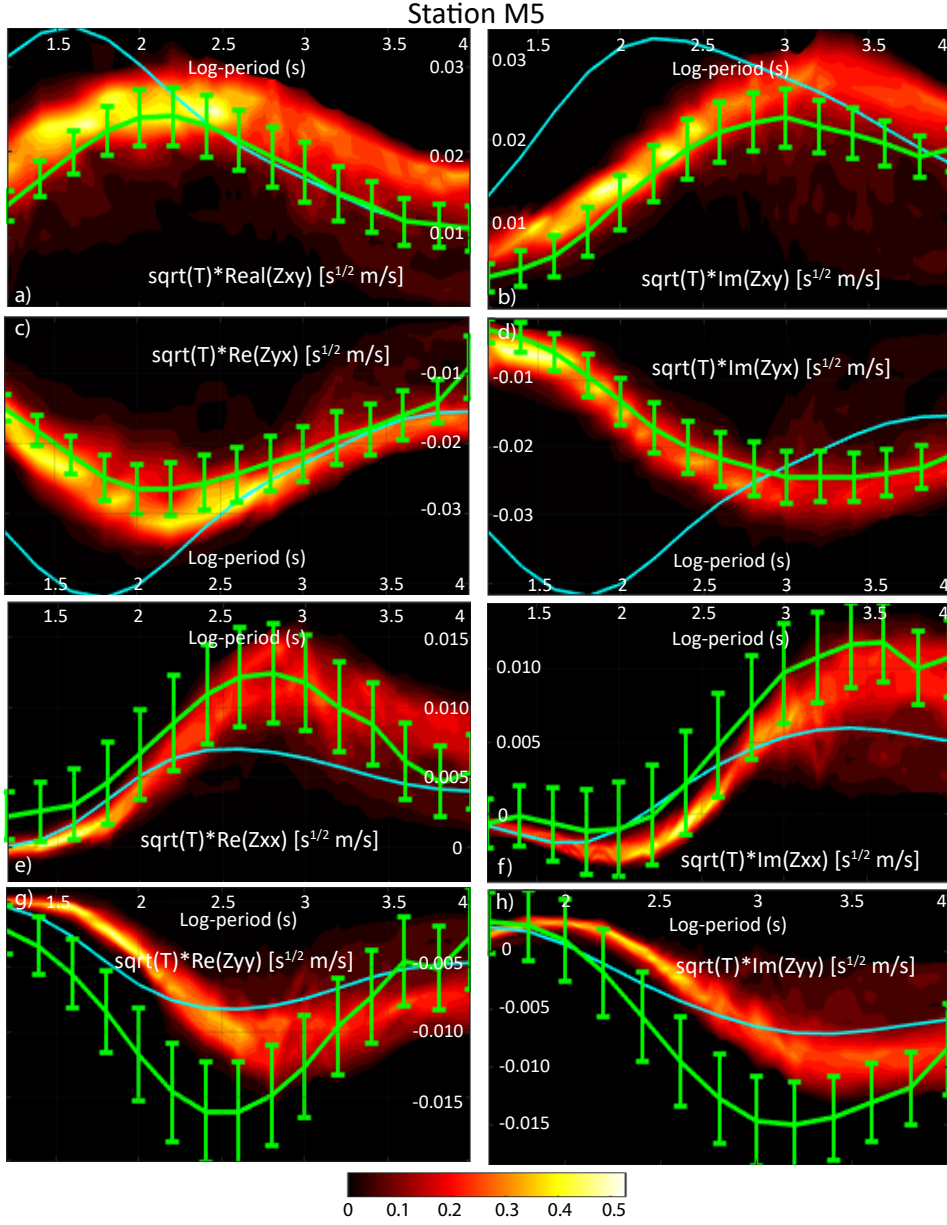


**Figure 2.** Posterior PDFs (refer to next section) of MT data for station M5. Field data and error bars are plotted in green and the computed data for the initial model is plotted in blue. Panels (a), (b), (c) and (d): Posterior PDFs of the real and imaginary parts of the off-diagonal components ( $Z_{xy}$  and  $Z_{yx}$ ). Panels (e), (f), (g) and (h): Posterior PDFs of the real and imaginary parts of the diagonal components ( $Z_{xx}$  and  $Z_{yy}$ ). The data has been scaled by the square-root of the period ( $T$ ) in all panels. The location of the station is shown in Figure 1.f

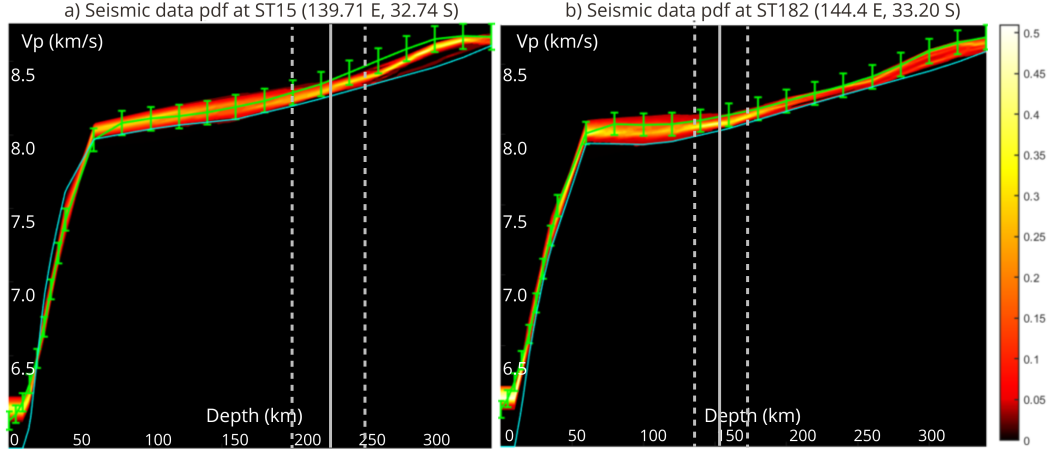


**Figure 3.** Posterior PDFs (refer to next section) of P-wave velocity data for stations (a) ST15 located at 139.71 E, 32.74 S and (b) ST182 at 144.4 E, 33.20 S. P-wave velocity data and error bars are plotted in green and the computed data for the initial model is plotted in blue. For those locations, the LAB depths corresponding to the mean, lower and upper bound of the 68% CI models are shown in solid and dashed grey lines, respectively.

where  $P(\mathbf{m})$  denotes the prior PDF describing all the information on the model’s parameters prior to the inversion (e.g., prior geological or petrological knowledge in the area of study).  $\mathcal{L}(\mathbf{m})$  is the likelihood function, which is specified by the statistical distribution of the data errors, and  $\phi$  is the *misfit* of model  $\mathbf{m}$ . In the case of MT, the data misfit is given by (Tarantola, 2005):

$$\phi = - \sum_{i=1}^N \frac{|g_i(\mathbf{m}) - d_i(\mathbf{m})|}{s_i}, \quad (2)$$

whereas the misfit for the seismic data takes the following form:

$$\phi = - \frac{1}{2} \sum_{i=1}^N \left( \frac{g_i(\mathbf{m}) - d_i(\mathbf{m})}{s_i} \right)^2. \quad (3)$$

For each data set,  $\mathbf{g}$  is the solution of a particular forward problem for model  $\mathbf{m}$ ,  $N$  is the total number of data and  $s_i$  denotes the standard deviation for the  $i$ -th data error.

The posterior PDF over data and parameters is commonly approximated using sampling-based Markov chain Monte Carlo (MCMC) algorithms (Gilks et al., 1995). In our joint inversions of independent data sets, we use the Delayed Rejection Adaptive Metropolis (DRAM) scheme of Haario et al. (2006) in combination with the Cascaded Metropolis (CM) approach (Tarantola, 2005; Hassani & Renaudin, 2013; Manassero et al., 2021). Details about the general inversion framework (RB+MCMC) are given in Manassero et al. (2021) while particular details about the sampling strategy, prior information and initial model used for the current inversion are given in Appendix A.

In order to define the model parameters of the inversion, we treat the conductivity and seismic velocities in the mantle as a superposition of two contributions: *background* properties related to the long-wavelength thermo-physical state of the dry mantle and *anomalous* conductivity features associated with the presence of water content, hydrous minerals, grain-boundary graphite films, interconnected sulfides, melts or metasomatized regions (Manassero et al., 2021). A particular realization of the background is defined

236 using a column-based parameterization which includes the depth to the thermal lithosphere-  
 237 asthenosphere boundary (LAB) and thermal nodes placed in the sub-lithospheric man-  
 238 tle of individual columns. This parameterization is used for both the seismic and MT  
 239 forward solution. We also use a second parameterization, within the MT problem only,  
 240 based on electrical conductivity nodes to account for the conductivity in the crust and  
 241 those conductivity anomalies over the background (see details in Appendix C and in Man-  
 242 assero et al., 2021).

243 We incorporate one conductivity cell below each MT station as an extra param-  
 244 eter of the inversion to account for the galvanic distortion effect produced by near-surface  
 245 inhomogeneities that are below the resolution of our model (Jones, 2011; Chave & Jones,  
 246 2012; Avdeeva et al., 2015). Similarly to the methodology used in ModEM (Kelbert et  
 247 al., 2014), these cells are placed in the first (thin) layer of the numerical mesh used to  
 248 solve the MT forward problem.

249 The crustal structure used within the seismic models consists of three crustal lay-  
 250 ers per column (upper crust/sediments, middle crust, and lower crust). Each layer has  
 251 a fixed thickness and its own set of physical properties: coefficient of thermal expansion,  
 252 isothermal compressibility, thermal conductivity, bulk density, volumetric radiogenic heat  
 253 production (RHP), thickness, P-wave ( $V_p$ ) and S-wave ( $V_s$ ) velocities, and  $V_p/V_s$  ratio.  
 254 Whilst all of these can be included as parameters of the inversion, in this work, the un-  
 255 knowns are the  $V_p$  of each crustal layer. The layers' densities are computed from  $V_p$  as-  
 256 suming Brocher's empirical law (Brocher, 2005) while  $V_s$  is obtained from the sampled  
 257  $V_p$  and the prior information on  $V_p/V_s$  ratios.

258 Information about the model parameters (i.e., LAB depths, temperature nodes,  $V_p$   
 259 velocity in the crust and conductivity nodes) and their uncertainties can be obtained by  
 260 exploring the posterior PDF. For example, we can estimate the mean model and the mod-  
 261 els corresponding with the lower and upper bounds of the 68 % confidence interval (CI)  
 262 of the posterior PDF. This interval corresponds with the range of models that fall within  
 263 one standard deviation from the mean, and is commonly used as an indicator of model  
 264 uncertainty. This complete information is later used to obtain models in terms of the thermo-  
 265 physical properties of the whole lithosphere, such as seismic velocities, electrical conduc-  
 266 tivity and water content.

### 267 3.3 Forward Problems and Model Discretization

268 Most of the forward problems solved during the probabilistic inversion (MT for-  
 269 ward in 3D, heat transfer and surface wave dispersion curves) have been described in de-  
 270 tail in Manassero et al. (2020, 2021) and in Afonso et al. (2013a, 2013b); Afonso, Rawl-  
 271 inson, et al. (2016). Subsequently, we focus on the model discretization and derivation  
 272 of the seismic velocity and background conductivity models from the model parameters.

273 The study area is subdivided into 441 columns of size  $0.45^\circ \times 0.45^\circ \times 410$  km, where  
 274 each column is discretized at three different scales:

- 275 1. The finest discretization scale makes up the fine mesh (2 km) to solve the seismic  
 276 forward operators (surface waves and seismic models) and the steady-state conduc-  
 277 tive geotherm in the lithosphere.
- 278 2. The intermediate discretization comprises the finite elements (FE) used to solve  
 279 the MT forward problem. In this case, we use  $63 \times 63 \times 36$  FE elements of size  
 280  $17 \times 17$  km in the horizontal and variable vertical size with depth. The air com-  
 281 prises four FE cells and a total thickness of 106 km.
- 282 3. The thermal nodes constitute the coarser discretization used to obtain mantle-stable  
 283 mineral assemblages and the corresponding physical properties (e.g., seismic ve-  
 284 locities, bulk density). In this study, the thermal nodes are placed every 50 km  
 285 in the vertical direction.



286 The thermo-physical properties at the thermal nodes are obtained by interpolat-  
 287 ing the properties from pre-computed tables at the nodes' specific composition, sampled  
 288 temperature and pressure (computed using a quadratic lithostatic-type approximation,  
 289 see Appendix B). In order to compute these tables, we use components of the software  
 290 PerpleX (Connolly, 2009; Afonso et al., 2013b) to solve the Gibbs free-energy minimiza-  
 291 tion problem together with the database and thermodynamic formalism of Stixrude &  
 292 Lithgow-Bertelloni (2011) within the CFMAS system ( $CaO - FeO - MgO - Al_2O_3 -$   
 293  $SiO_2$ ). All thermophysical properties computed at the thermodynamic nodes are linearly  
 294 interpolated to the fine mesh for the computation of the seismic forward operator and  
 295 to the FE mesh for the computation of the MT forward solution (see details in Appendix  
 296 B).

### 297 3.4 Mantle composition

298 The equilibrium assemblages are computed using a mean bulk mantle composition  
 299 (i.e., specific CFMAS compositions) of 44.3 wt%  $SiO_2$ , 2.8 wt%  $Al_2O_3$ , 8.5 wt%  $Fe_2O_3$ ,  
 300 39.3 wt%  $MgO$  and 2.7 wt%  $CaO$ . We estimate this mean composition by averaging eight  
 301 spinel lherzolites xenoliths (see Table S1 in Supplementary material) that were entrained  
 302 in EAVP lavas. We use major element compositions from Irving (1980), O'Reilly & Grif-  
 303 fin (1987), Griffin et al. (1987) and unreported samples from Bokhara River (J. Shea,  
 304 personal communications), which cover the area of interest. Since this is the most re-  
 305 cent volcanism in eastern Australia, these xenoliths are the most representative samples  
 306 of current mantle compositions available.

307 The vast majority of xenoliths in eastern Australia equilibrated at pressures  $< 2$   
 308 GPa (O'Reilly & Griffin, 1985; Pearson et al., 1991; Sutherland et al., 1994). However,  
 309 the CFMAS compositions used here are close to the continental mantle (McDonough,  
 310 1990): fertile peridotites (Boyd, 1989b) and pyrolite (Ringwood, 1962). Suggesting these  
 311 xenoliths have not been modally metasomatized, and their CFMAS concentrations are  
 312 equilibrated with upper mantle peridotites, which allows for their average to be used as  
 313 an estimate for current mantle compositions beneath eastern Australia. We note that  
 314 in cratonic regions, the average mantle compositions may resemble harzburgitic or dunitic  
 315 compositions (Boyd, 1989b).

316 The use of an average mantle composition is justified by the fact that the seismic  
 317 velocities and electrical conductivity have second-order sensitivity to dry bulk mantle  
 318 composition (see Figure S1, S2 and Özaydın & Selway, 2020; Trampert et al., 2001; Goes  
 319 et al., 2000). We also assume a dry mantle composition for the background properties.  
 320 The reason for this is that, firstly, the seismic velocities are not affected by small amounts  
 321 of water commonly observed in mantle samples (Yu et al., 2011, and references therein)  
 322 as the actual phase compositions are insensitive to water contents bound to minerals (Cline Ii  
 323 et al., 2018). Secondly, since the conductivity nodes represent any conductivity value that  
 324 departs from the background (dry resistive mantle), this choice allows us to sample only  
 325 positive anomalies and reduce the number of parameters by two (see Manassero et al.,  
 326 2021).

### 327 3.5 Mantle water content

328 Using outputs of the joint probabilistic inversion (thermal structure and conduc-  
 329 tivity models) and the mean mantle composition described above, we obtain estimations  
 330 of the bulk water content in the mantle (i.e. hydroxyl or  $OH^-$  bound to nominally an-  
 331 hydrous minerals) as a proxy for mantle metasomatism. These estimations are made us-  
 332 ing the software MATE (Özaydın & Selway, 2020), which includes several experimen-  
 333 tal models for electrical conductivity, water partitioning and solubility (based on petro-  
 334 logical studies). In particular, we used the electrical conductivity models of Gardés et

335 al. (2014a), Dai & Karato (2009a), Liu et al. (2019), and Dai & Karato (2009c) for olivine,  
 336 orthopyroxene, clinopyroxene and garnet, respectively.

337 The solutions for the water content lie between the bounds defined by the dry litho-  
 338 sphere (i.e., 0 ppm) and the maximum bulk water content calculated using the olivine  
 339 water solubility model of Padrón-Navarta & Hermann (2017). The experimental coef-  
 340 ficients used in the water partitioning are:  $D_{opx/ol}^{OH} = 5.6$ ,  $D_{cpx/opx}^{OH} = 1.9$  of Demouchy  
 341 et al. (2017) and  $D_{gt/ol}^{OH} = 0.8$  of Novella et al. (2014); which reflect the sub-solidus con-  
 342 ditions found in the continental lithospheric mantle in southeastern Australia. Since we  
 343 aim to portray variations of water content in the mantle rather than fitting the real wa-  
 344 ter content seen in xenoliths, the choice of the experimental parameters is adequate for  
 345 our calculations. All water calculations are made using the calibration of Withers et al.  
 346 (2012) for olivine, and the calibration of Bell et al. (1995) for pyroxenes and garnet.

347 The electrical conductivity of each individual phase is turned into bulk conductiv-  
 348 ity through the Generalised Archie's Law (Glover, 2010) with cementation components  
 349 ( $m$ ) of  $m = 2$  for orthopyroxenes,  $m = 4$  for clinopyroxenes and garnet, and  $m < 1$   
 350 for olivine (perfectly connected). The Generalised Archie's Law is preferred over the con-  
 351 servative estimates of Hashin-Shtrikman lower-bound since it allows us to incorporate  
 352 the effects of specific minerals in the conductivity values, such as highly-interconnected  
 353 phlogopites. The main cementation components used here, however, provide similar val-  
 354 ues to the Hashin-Shtrikman lower-bound for a lherzolitic matrix (Özaydın & Selway,  
 355 2020).

## 356 4 Results

### 357 4.1 Thermal structure of Southeast Australia

358 The depth to the thermal LAB ( $1250^{\circ}C$ , Afonso, Rawlinson, et al., 2016) obtained  
 359 from the joint probabilistic inversion of seismic velocities and MT data is shown in Fig-  
 360 ure 4, while the complete 3D temperature structure is shown via depth slices in Figure  
 361 5 (first three columns). Figure 4 also includes a recent LAB model obtained from a 1D  
 362 joint probabilistic inversion of elevation, surface heat flow, Rayleigh wave dispersion curves,  
 363 and geoid anomalies using LitMod1D (Haynes et al., 2020; Afonso et al., 2013b); and the  
 364 estimated LAB depths from two recent seismic tomography models in eastern Australia  
 365 (Davies et al., 2015; Rawlinson et al., 2017). These results reveal a highly heterogeneous  
 366 lithospheric structure beneath the Tasmanides: while shallow LAB depths ( $< 100$  km)  
 367 are imaged on the eastern and south edges of the model, deeper LAB depths ( $> 250$  km)  
 368 are found beneath the Curnamona Province (CP) and the northern part of the Delame-  
 369 rian Orogen. We observe that the lithospheric structure is also in agreement with the  
 370 locations of recent volcanism (e.g., Figure 4.a): the leucitite volcanic centers correlate  
 371 with regions of an intermediate lithospheric thickness (125-160km) while the basaltic vol-  
 372 canoes are located in regions where the LAB depth is less than 120 km. The most dis-  
 373 tinctive features are step-like changes in the LAB depth from the CP to the southeast  
 374 corner of the model.

375 The LAB model is in good agreement with the mean LAB obtained using LitMod1D  
 376 (Afonso et al., 2013a, 2013b; Haynes et al., 2020), even though the data sets used in each  
 377 inversion are completely different. The first-order LAB structure is also in agreement with  
 378 the LAB depths derived from seismic velocity models (Davies et al., 2015; Rawlinson et  
 379 al., 2017). In particular, we observe similar LAB depths beneath the basaltic volcanoes  
 380 and west of  $146^{\circ}E$ , where a wedge-like structure follows the curvature of the Stawell Zone  
 381 (SZ, see Figure 3.1). There is a clear discrepancy in the center of the models where our  
 382 inversion yields shallower mean LAB depths ( $< 150$  km). The LAB of Davies et al. (2015)  
 383 falls, however, within the model uncertainties of our inversion. Even though we use the  
 384 model of Rawlinson et al. (2016) as data, the reason for this discrepancy is that our in-

385 version directly samples temperature and favors dynamic features (instead of a thick con-  
 386 ductive LAB) in order to fit all constraining data sets simultaneously.

387 The main difference between our LAB depths and the models of (Davies et al., 2015;  
 388 Rawlinson et al., 2017) is that we observe deeper LAB depths beneath CP. At first, this  
 389 difference could be attributed to the fact that the composition in this cratonic area is  
 390 more depleted than the average bulk mantle composition used here (see Section 3.3) and  
 391 deeper LAB depths are needed to fit the fast seismic velocities in this region. However,  
 392 the seismic velocities computed for a cratonic composition (abyssal peridotite after Boyd,  
 393 1989a) are comparable to those computed with the average bulk composition used in the  
 394 lithosphere (Figure S3a, Supplementary Material). Given the good data fit for the seis-  
 395 mic velocities in the region (Figure S3b), we note that the LAB depths found beneath  
 396 CP are consistent with the Paleoproterozoic-Archean origins of this cratonic region (Page  
 397 et al., 2005; Hand et al., 2008).

398 The depths to the thermal LABs obtained after an RB+MCMC probabilistic in-  
 399 version using MT data only are shown in Figures 6. Compared to the results from the  
 400 joint inversion, these figures show large variability and lack of structure in the LAB mod-  
 401 els. This comparison elucidates the fact that MT alone provides low sensitivity to dis-  
 402 criminate the temperature from other factors controlling the conductivity. Given the poor  
 403 constraints provided by MT, it becomes evident that other types of data sets (e.g., seis-  
 404 mic) are necessary to image the thermal lithospheric structure properly.

## 405 4.2 Seismic velocity structure

406 Depth slices of the P-wave velocity structure predicted by our model are shown in  
 407 Figure 5. The P-wave velocity model of Rawlinson et al. (2016) is also included as a ref-  
 408 erence. In all cases, the velocities are plotted relative to the AusREM model at  $34.4^{\circ}S, 145^{\circ}E$   
 409 (Figure S4 in Supplementary Material). We observe that the inversion succeeded in re-  
 410 producing the  $V_p$  structure found in the model of Rawlinson et al. (2016). In particu-  
 411 lar, the mean P-wave velocity down to 100 km is practically identical in both models.  
 412 Interestingly, the Newer Volcanic province stands out as a low-velocity anomaly at depths  
 413 between 60 and 80 km. On the other hand, the basaltic volcanoes in the middle of the  
 414 Eastern Province ( $\sim 149^{\circ}E, 34^{\circ}S$ ) correlate well with deep low-velocity anomalies.

415 Some minor discrepancies are observed at depths below 100 km between our re-  
 416 sults and the model of Rawlinson et al. (2016). For instance, we obtain slightly higher  
 417 seismic velocities (0.6% higher on average) at depths from 100 to 180 km at the east-  
 418 ern end of the model. Whilst most of these differences fall within the model uncertain-  
 419 ties, they can be mostly attributed to the constraints imposed by the MT in the joint  
 420 inversion. Similarly, we obtain slightly slower velocities throughout the whole model at  
 421 200-220 km depth (see Figure 5). At these depths, the local discrepancies are simply ex-  
 422 plained by the use of different physical parameterizations.

## 423 4.3 Electrical conductivity structure

424 The conductivity models for the crust and mantle predicted by the joint inversion  
 425 are shown in Figures 7, 8 and 9. For comparison, these figures include the results ob-  
 426 tained from a recent deterministic inversion of MT data (Kirkby et al., 2020), using the  
 427 ModEM software (Kelbert et al., 2014). The main structures observed in the conduc-  
 428 tivity models are comparable (within model uncertainties) to those in the model of Kirkby  
 429 et al. (2020) at all depths.

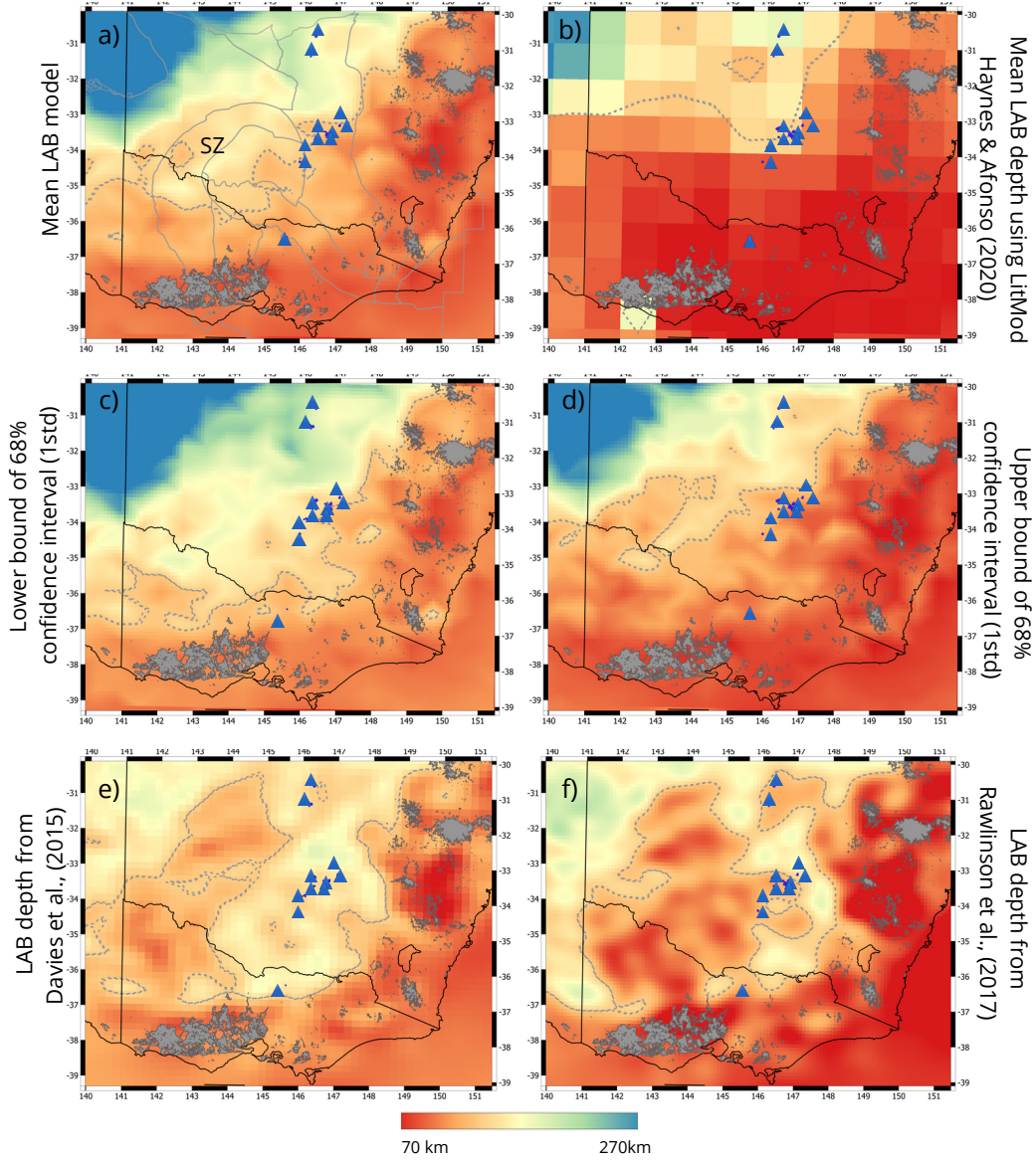


**Figure 4.** Depth of the thermal LAB. (a) Mean model after the joint probabilistic inversion; (b) mean model obtained after a 1D joint probabilistic inversion (Haynes et al., 2020; Afonso et al., 2013b); (c) and (d) lower and upper bounds of the 68 % confidence interval (1 standard deviation from the mean), respectively. (e) and (f) depth of the LAB after Rawlinson et al. (2017) and Davies et al. (2015), respectively. The location of leucitite-bearing volcanism are shown in blue and standard basaltic volcanoes in grey. The 140 km-contour of the LAB depth is shown in dashed-grey line and the outline of the tectonic provinces in solid grey lines. The location of the Stawell Zone (SZ) is marked in panel (a).



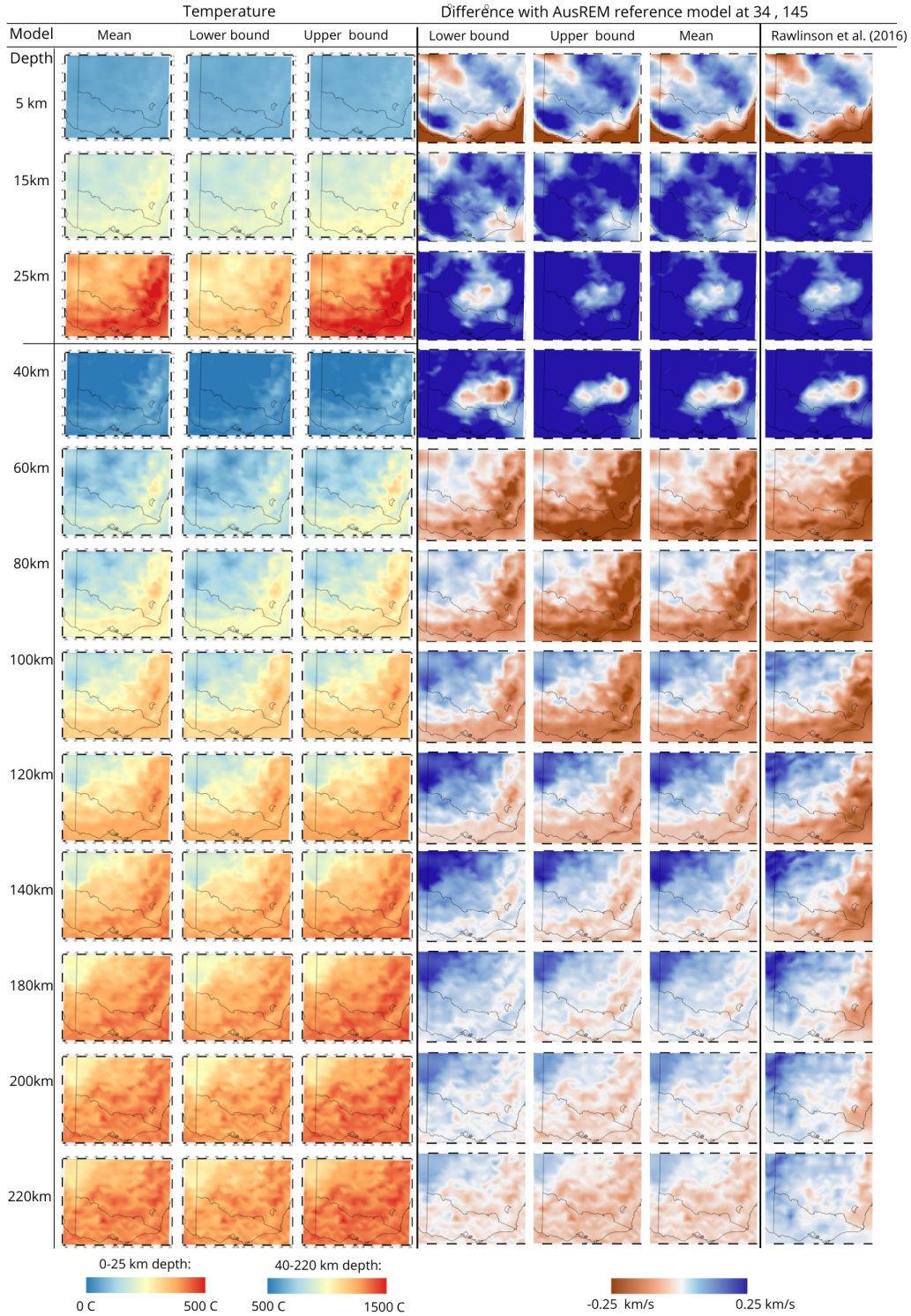


**Figure 5.** Columns (1)-(3): depth slices from the (1) mean model and those models corresponding to (2) the lower and (3) upper bound of the 68% CI of the posterior PDF for the temperature. Columns (4)-(6): depth slices from the models corresponding to (4) the lower and (5) upper bound of the 68% CI, and (6) mean of the posterior PDF for the P-wave velocity; Column (7): P-wave velocity model of (Rawlinson et al., 2016). Selected depths are shown on the left of the figure. In all cases, velocities are plotted relative to 1-D reference model AusREM at  $34.4^{\circ}S, 145^{\circ}E$  shown in Figure S4 of the Supplementary Material.

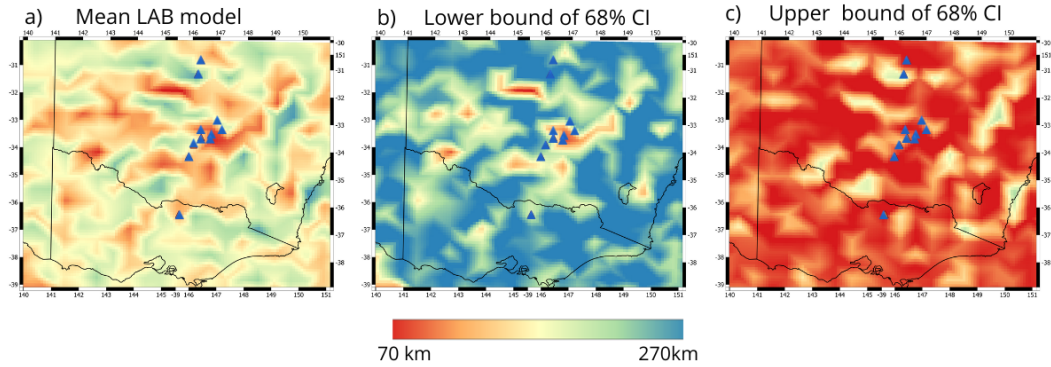


**Figure 6.** LAB depth from a probabilistic inversion of MT data only. (a) Mean, (b) lower and (c) upper bounds of the 68 % confidence interval. The location of leucite volcanoes are shown in blue triangles.

430

### 4.3.1 Crust

431

432

433

434

435

436

437

438

439

440

441

442

443

444

Figures 10 indicate the agreement between the conductivity structure in the crust and independent information: sedimentary basins (Raymond et al., 2012), magnetic anomalies (Nakamura & Milligan, 2015) and a shear velocity model (Pilia et al., 2015). In particular, Panel (a) shows that the extent of the Paleozoic to Cenozoic sedimentary basins in the region is well outlined by the mean conductivity model at 2 km depth. A visual comparison between Panels (c,e,f) and Panel (b) shows the correlation between total magnetic anomalies and conductivity features at different depths. Examples of these are (A) a conductor in the CP; (B) a SW-NE linear structure close to the NW limit of Murray Basin; conductors (C) and (D) in the Tabberabbera Zone; (E) a N-S conductor aligned with the western border of the Eastern Province; (F) two resistive structures west of the Sydney Basin; (G) the Sydney Basin; (H) a conductive region aligned with the north limit of the Northwest and Central NSW provinces; (I) a highly resistive region in the Stawell Zone near the NSW-VIC border; (J) a circular structure in the middle of the model; (K) a high-conductivity anomaly; and (L) a conductor east of CP.

445

446

447

448

449

450

451

452

453

The conductor (A) correlates well with the conductor seen in the MT study of Robertson et al. (2016), using data from 74 AusLAMP stations placed in the Ikara–Flinders Ranges and CP, and in the recent study of Kay et al. (2022), using a densely-spaced MT modeling scheme. Comparing Panels (c) and (d), we observe that the structures (A)-(G) correlate well with low and high-velocity regions imaged by the shear-wave velocity model of Pilia et al. (2015). We note that the concentric geometries at 29 km depth, such as conductor (J) and structures on the west of the model, resemble the features of the Lachlan Orocline model revealed by potential field and passive seismic data (c.f. Kirkby et al., 2020).

454

### 4.3.2 Mantle

455

456

457

458

459

The similarities between the mantle conductivity models at  $\sim 40$ -80 km depth and features found in the gravity anomalies (Nakamura, 2016) are shown in Figures 11. These features are: the conductor (A); a conductor (M) in the northwest of the Tabberabbera Zone; two conductivity lineaments (N and O); and a linear conductor (P) placed at the border between the Stawell Zone and the Delamerian Orogen.

460

461

The conductivity models between 80-250 km depth (Figures 8 and 9) largely resemble the ModEM model of Kirkby et al. (2020). In particular, we observe a similar

462 north-eastward orientation of the conductors in the middle of the model ( $C_1, C_2, C_3, C_4$   
 463 and  $C_5$  in Figure 9). Comparing the mantle conductivity with the mean LAB structure  
 464 in (Figures 12), our models suggest that there is a good alignment between the LAB to-  
 465 pography and these mantle conductors (cf. Kirkby et al., 2020). Notably,  $C_5$  aligns well  
 466 with the LAB wedge northwest of the model,  $C_{3N}$  and  $C_{4S}$  follow the 140 km LAB depth  
 467 iso-surface while  $C_1, C_2$  and  $C_{3S}$  align with LAB depths  $< 120$  km. We also observe a  
 468 deep high-conductivity structure beneath the CP ( $C_6$ ), which agrees well with the struc-  
 469 ture imaged by previous MT studies (e.g., Robertson et al., 2016; Thiel & Heinson, 2013).  
 470 A high-conductivity region ( $C_4$ ) is observed below the central-leucitite volcanoes. In our  
 471 models, the extent of this region is larger and more connected than in the ModEM model.

472 The main difference we observe between our conductivity model and the model Kirkby  
 473 et al. (2020) is that the sub-lithospheric conductivities along the south-east coast and  
 474 in the middle of the model are higher than those values found in the model of Kirkby  
 475 et al. (2020) ( $R_1$  and  $R_2$  in Figures 9) and in the models from a probabilistic inversion  
 476 of MT data only (Figure S5, Supplementary Material). The high resistivity ( $> 10^4 \Omega m$   
 477 ) in these regions have been at odds with the mantle resistivity range obtained for sub-  
 478 lithospheric temperatures and pressures (Fullea et al., 2011; Naif et al., 2021). We ob-  
 479 serve that, due to the favorable constraint of the seismic data to the thermal structure  
 480 in the joint probabilistic inversion, these high resistivity values are not permissive any-  
 481 more.

482 Another example of the favorable constraint imposed by the seismic data in the con-  
 483 ductivity models is shown in Figures 12. At 140 km depth, we observe that the conduc-  
 484 tors in the east ( $C_1, C_2$  and  $C_{3S}$  in Figure 12.c) are located within a region defined by  
 485 a  $1250^\circ\text{C}$ -contour (Figure 12.b). These mantle conductivity structures correlate well with  
 486 both the location of the eastern basaltic volcanics and a stripe of low P-wave seismic ve-  
 487 locities (Figure 12.d). At the same time, the stripe of high seismic velocities beneath the  
 488 east coast at a depth of 140 km is a clear example of the constraint imposed by the MT  
 489 data in the velocity models. This stripe is not seen in the models of Rawlinson et al. (2016)  
 490 and correlates with a relatively cold and highly resistive mantle (Figures 12.b-c).

#### 491 **4.4 Joint assessment of bulk water content and temperature maps**

492 One of the key benefits of our inversion is that we can dissociate the effects of the  
 493 temperature and other factors controlling the conductivity structures, such as water con-  
 494 tent. The bulk water content maps derived from the mantle conductivity models are shown  
 495 in Figures 13 and 14. We observe that most of the localized conductive anomalies above  
 496 the background are likely to contain high percentages of bulk water content. This is the  
 497 case for the following structures depicted in Figure 14:  $C_1, C_2$  and  $C_3$  beneath the east-  
 498 ern basaltic volcanoes;  $C_4$  below the central leucitites;  $C_5$  on the eastern boundary of  
 499 Delamerian Orogen;  $C_6$  beneath CP; and the deep localized conductor  $C_7$  at  $\sim -30.5^\circ N, 147^\circ E$ .

500 Figures 15-17 and Figure S6 show vertical slices of the conductivity, water content  
 501 and temperature along four transects depicted in Panel (b) of Figure 12. The transects  
 502 in Figure 15 cross most of the geological provinces on the west and demonstrate a strik-  
 503 ing correlation between the geological boundaries and the alternation between wet/dry  
 504 portions of the lithosphere. The joint assessment of these transects clearly shows that  
 505 the lithospheric mantle beneath CP ( $C_6$ ) corresponds with a highly conductive, hydrated,  
 506 and cold region. We observe a high-conductivity anomaly ( $C_5$ ) below the Stawell Zone  
 507 that crosses the LAB. While the high temperatures found in this region ( $T_2$  in Figure  
 508 15c) can partially explain the conductivity of this structure, Figure 15b indicates that  
 509 a large part of its conductivity is related to the presence of water content. Similarly, the  
 510 high-conductivities observed in the region  $C_{3N}$  (beneath Tabberrabbera Zone) and the  
 511 conductor  $C_{NV1}$  (at  $\sim 90$  km depth beneath the NV) are entirely explained by a large  
 512 amount of water content.



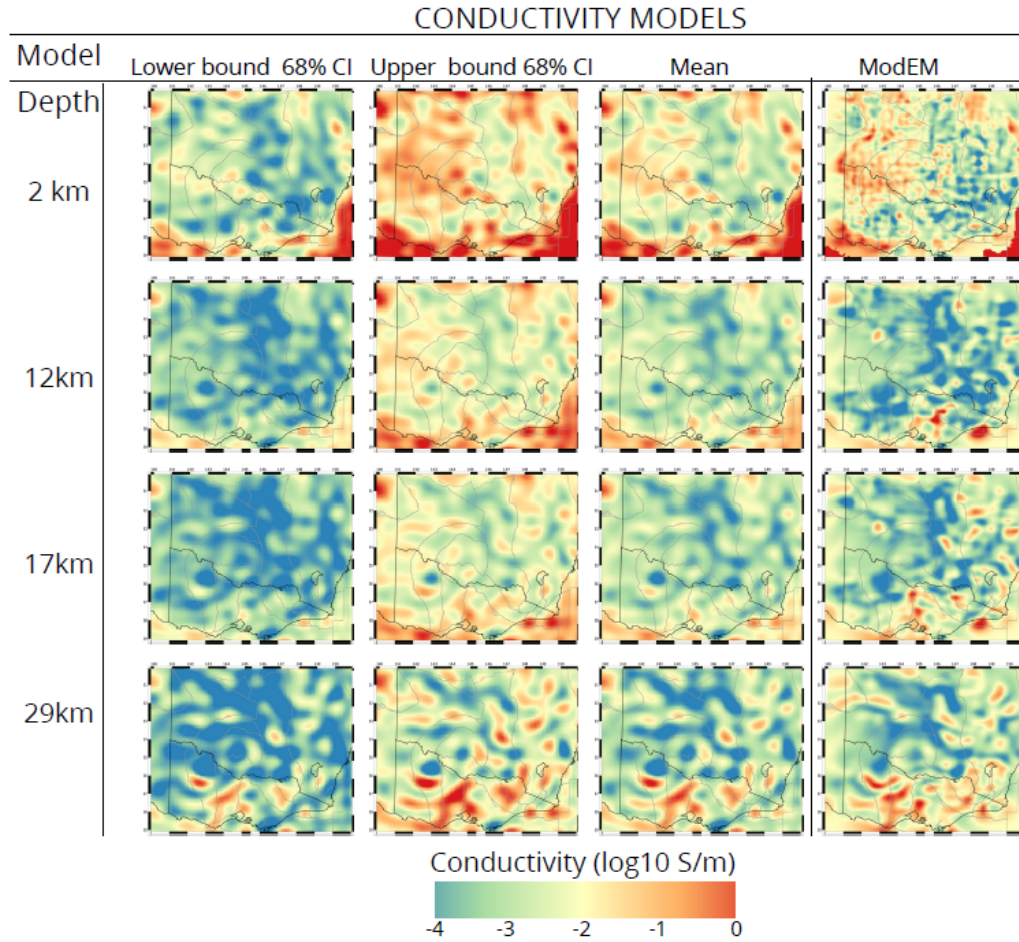


**Figure 7.** Conductivity in the crust from the joint probabilistic inversion. Columns (1)-(3): depth slices from the (1) the lower, (2) upper bound of the 68% percentile and (3) mean conductivity models of the posterior PDF. Column (4): conductivity model of (Kirkby et al., 2020). Selected depths are shown on the left of the figure and the boundaries of geological provinces are shown in grey lines.



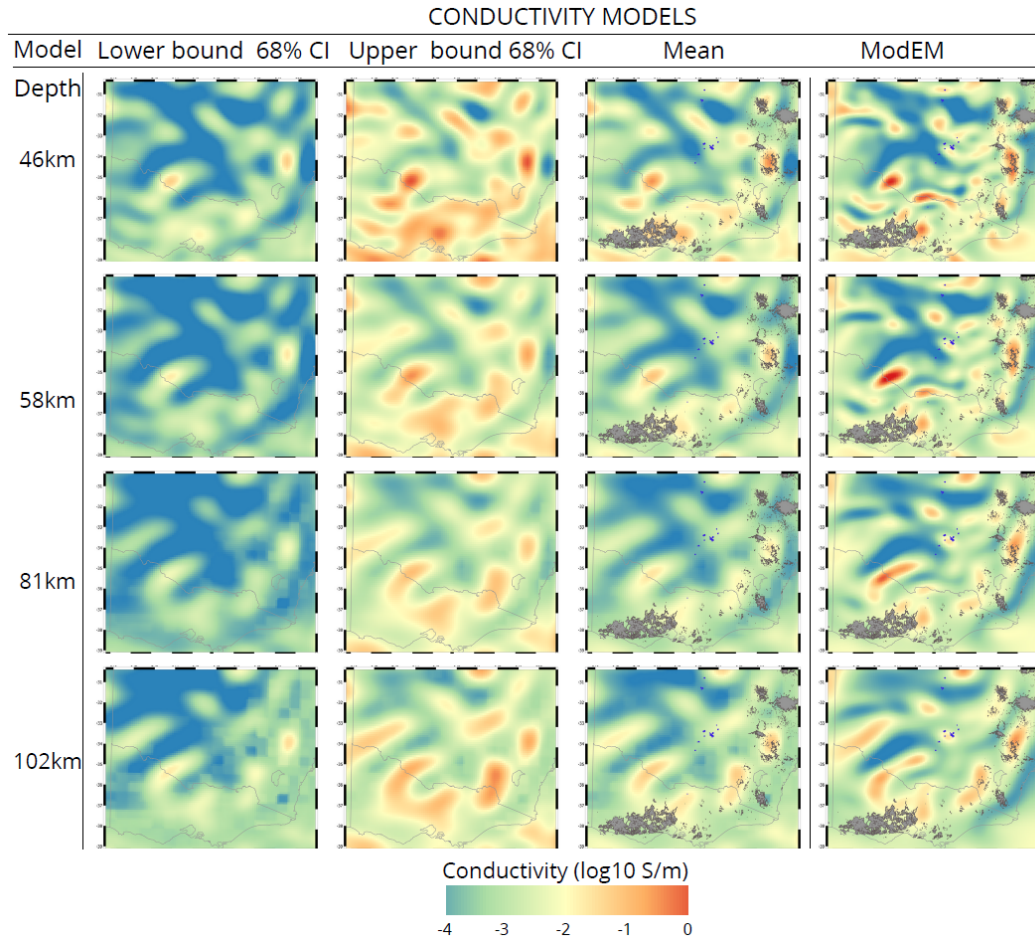


**Figure 8.** Mantle conductivity from the joint probabilistic inversion. Columns (1)-(3): depth slices from the (1) the lower, (2) upper bound of the 68% percentile and (3) mean conductivity models of the posterior PDF. Column (4): conductivity model of Kirkby et al. (2020). The location of leucitite-bearing volcanism are shown in blue and standard basaltic volcanoes in grey. Selected depths are shown on the left of the figure.

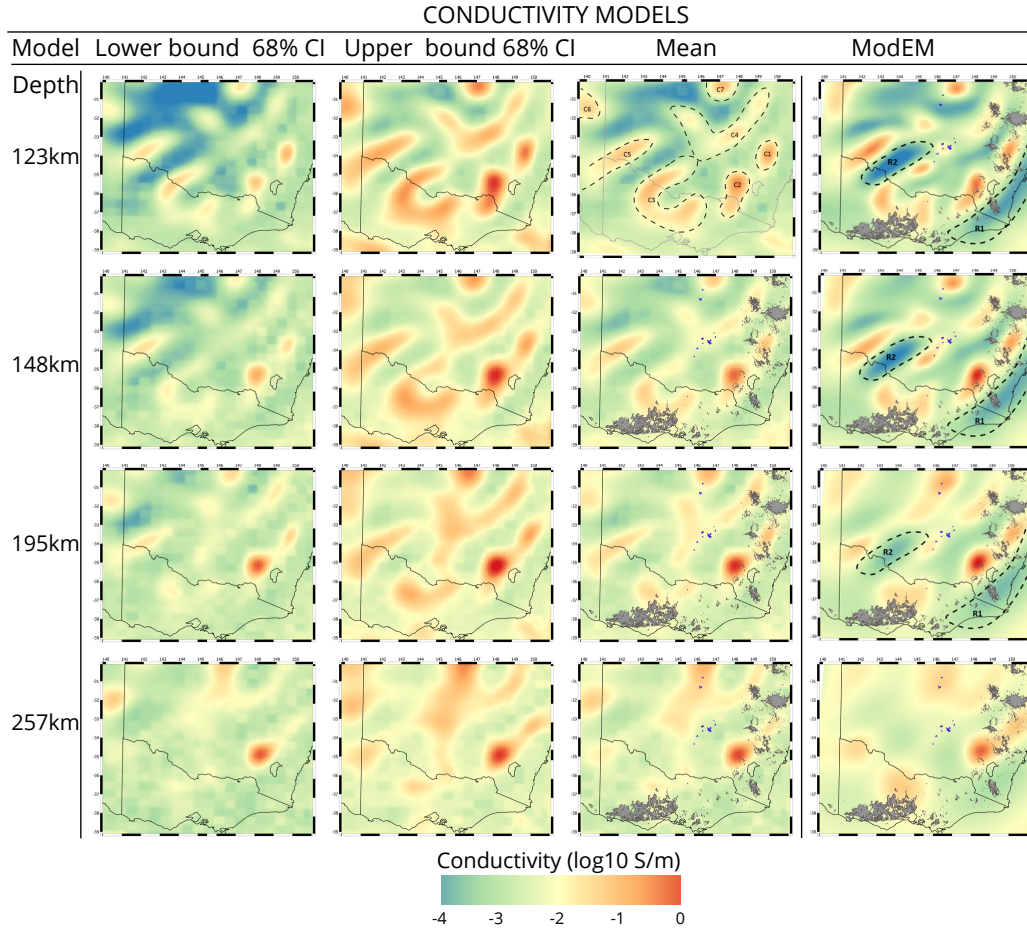


**Figure 9.** Mantle conductivity from the joint probabilistic inversion. Columns (1)-(3): depth slices from the (1) the lower, (2) upper bound of the 68% percentile and (3) mean conductivity models of the posterior PDF. Column (4): conductivity model of Kirkby et al. (2020). The location of leucitite-bearing volcanism are shown in blue and standard basaltic volcanoes in grey. Selected depths are shown on the left of the figure. Dashed-black lines highlight conductors in the mean model and resistors in the ModEM model at 123 km depth.

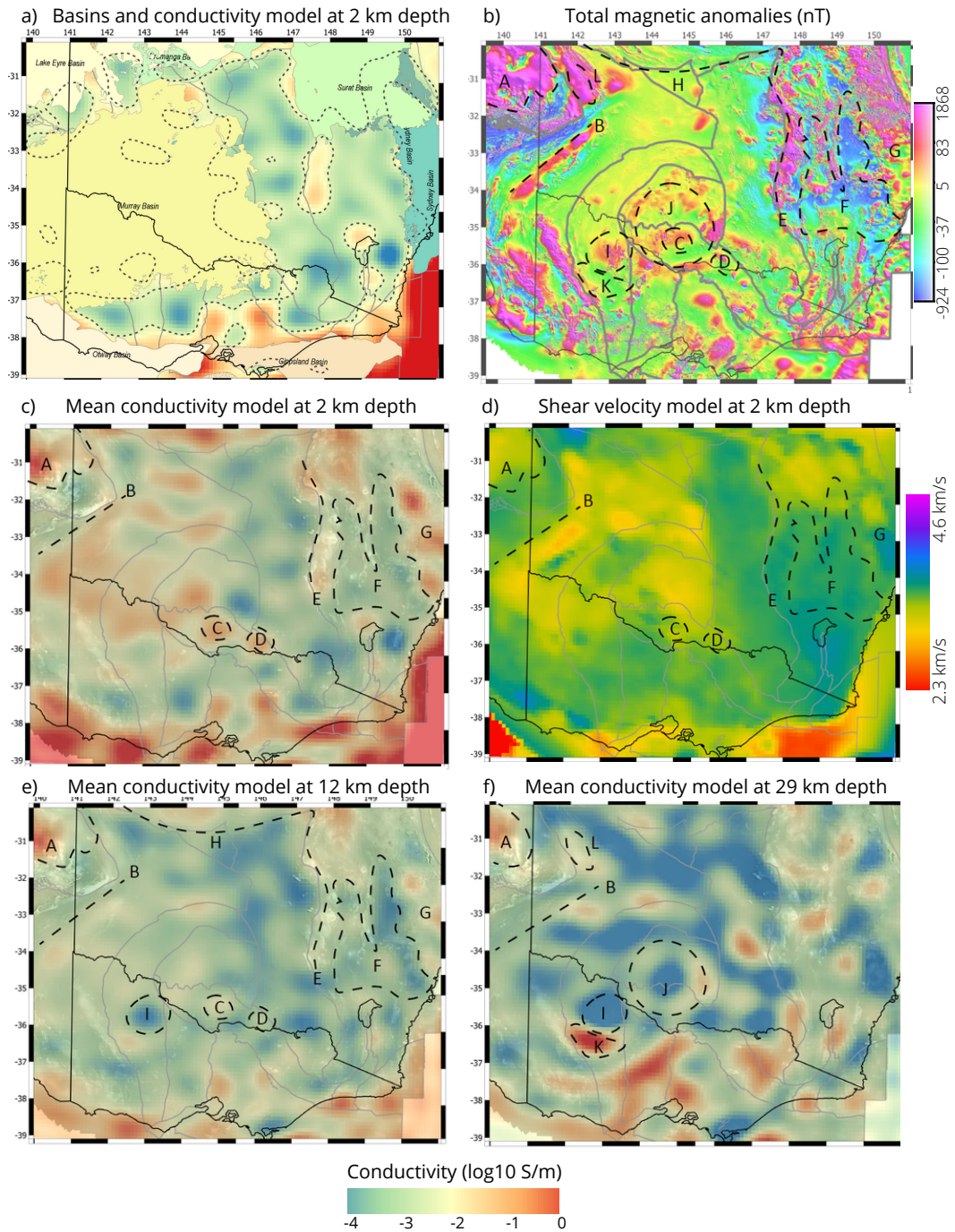


**Figure 10.** (a) Sedimentary basins overlying mean conductivity model at 2 km depth and 200  $\Omega m$ -resistivity contour in dash lines. (b) Total magnetic anomalies after Nakamura & Milligan (2015) (c) Mean conductivity and (d) share wave velocity model after Pilia et al. (2015) at 2 km depth. (e-f) Mean conductivity models at 12 and 29 km depth. We refer the reader to the main text for a description of structures A-L. Boundaries of geological provinces are shown in grey lines.



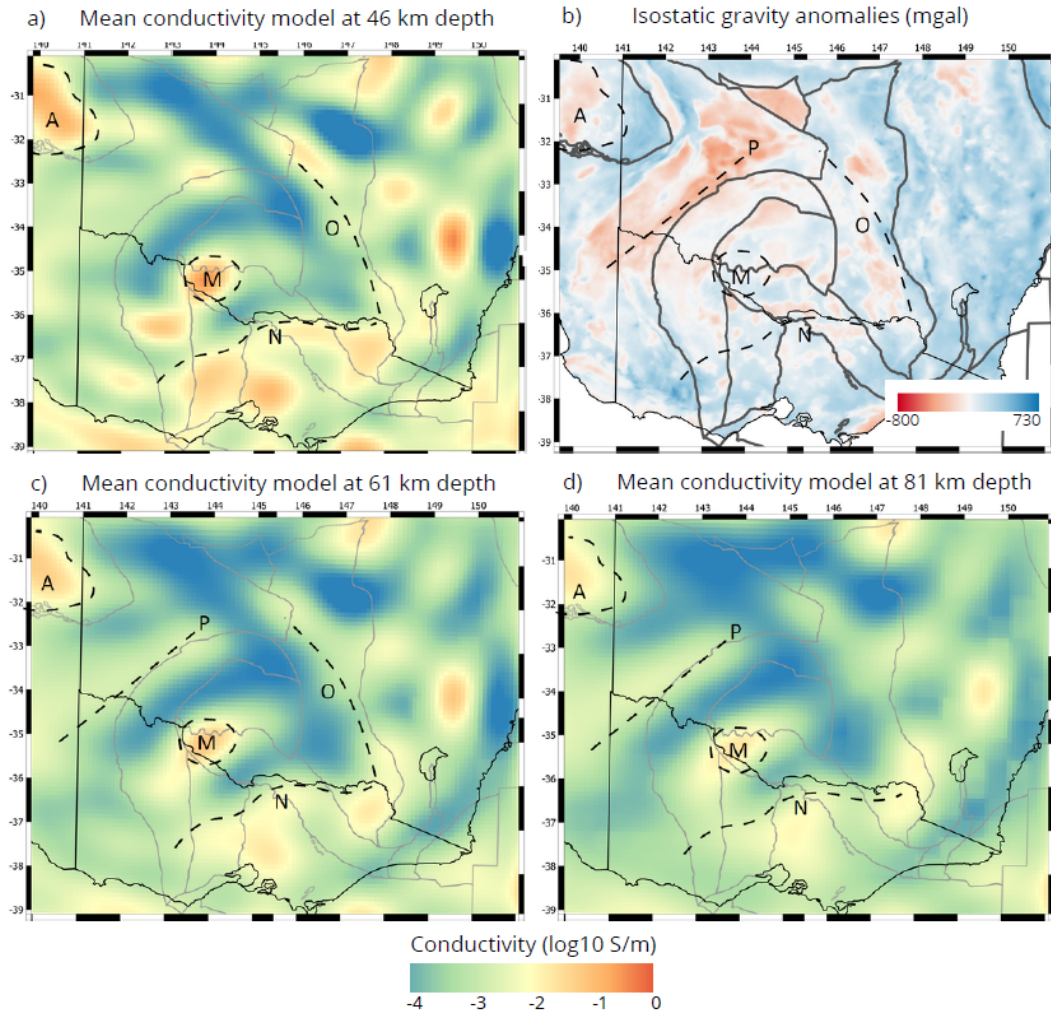


**Figure 11.** (a), (c) and (d) Mean conductivity models at 46, 61 and 81 km depth, respectively. (b) Isostatic gravity anomalies after Nakamura (2016). We refer the reader to the main text for a description of structures M-P. Boundaries of geological provinces are shown in grey lines.

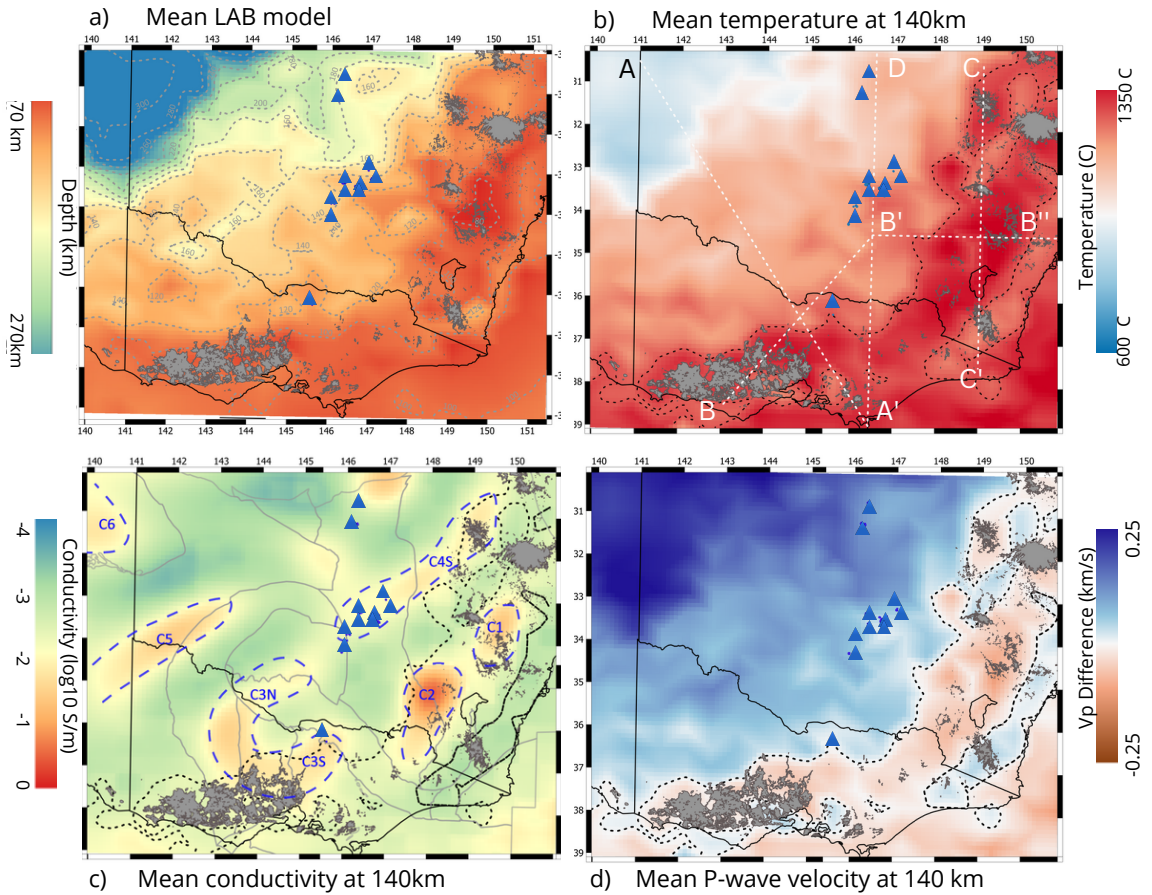


**Figure 12.** (a) Mean LAB depth. Contours of the LAB depth every 20 km are shown in grey-dashed line. Mean models at 140 km of (b) temperature (c) electrical conductivity and (d) P-wave velocity relative to 1-D reference model AusREM at  $34.4^{\circ}S, 145^{\circ}E$ . The  $1250^{\circ}C$ -contour (corresponding with the thermal LAB) is plotted in dashed-black in (b-d). Panel (c) shows the location of the geological provinces and conductors in dashed blue. The location of leucite volcanoes are shown in blue triangles and the surface outcrop of basaltic volcanics are shown in grey in all panels. Panel (b) shows five transects which are discussed in section 5.1.

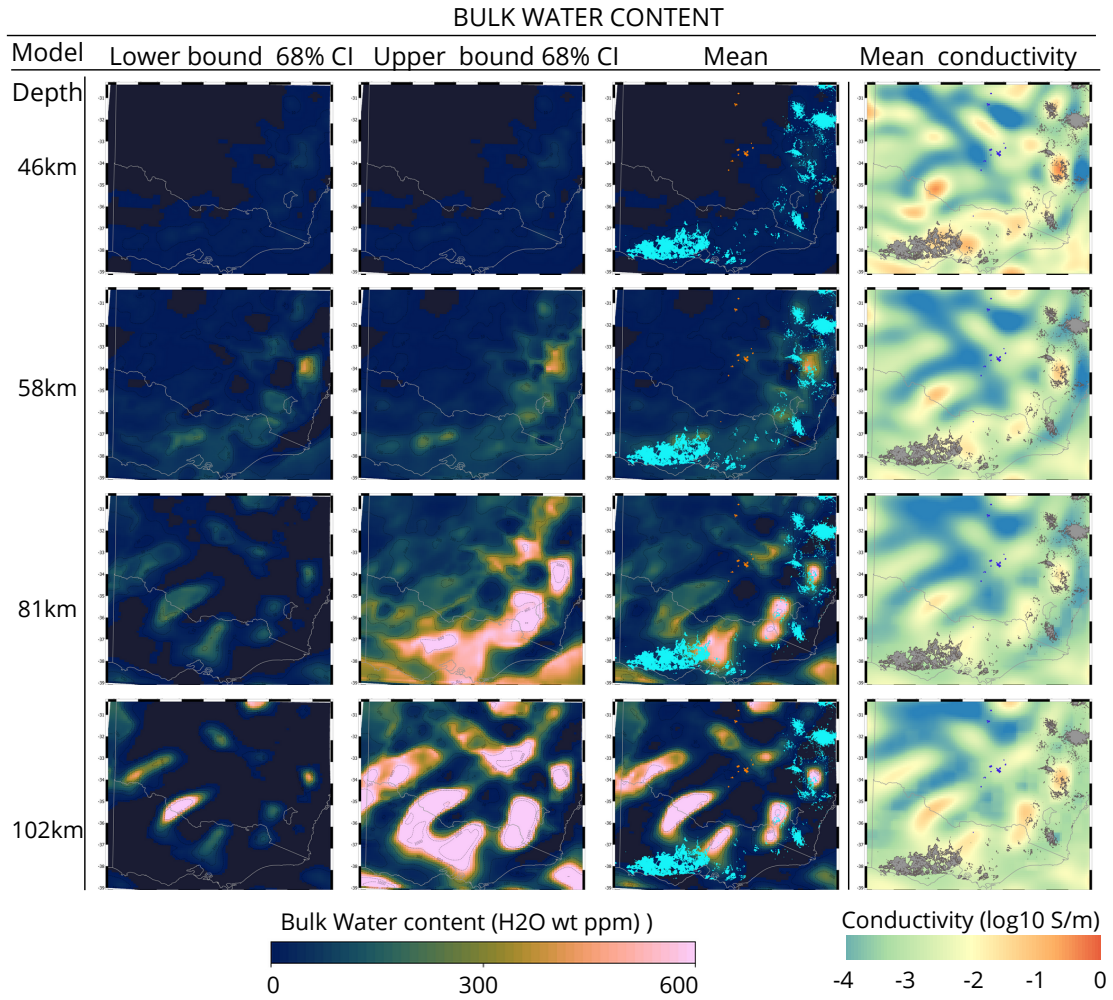


**Figure 13.** Bulk water content and mantle conductivity models from the joint probabilistic inversion. Columns (1)-(3): water content maps obtained from the (1) the lower, (2) upper bound of the 68% CI and (3) mean conductivity models. Column (4): depth slices from mean conductivity models of the posterior PDF. The location of leucitite-bearing volcanism and basaltic volcanoes are shown in orange and turquoise in (3); and blue and in grey in (4). Selected depths are shown on the left of the figure.

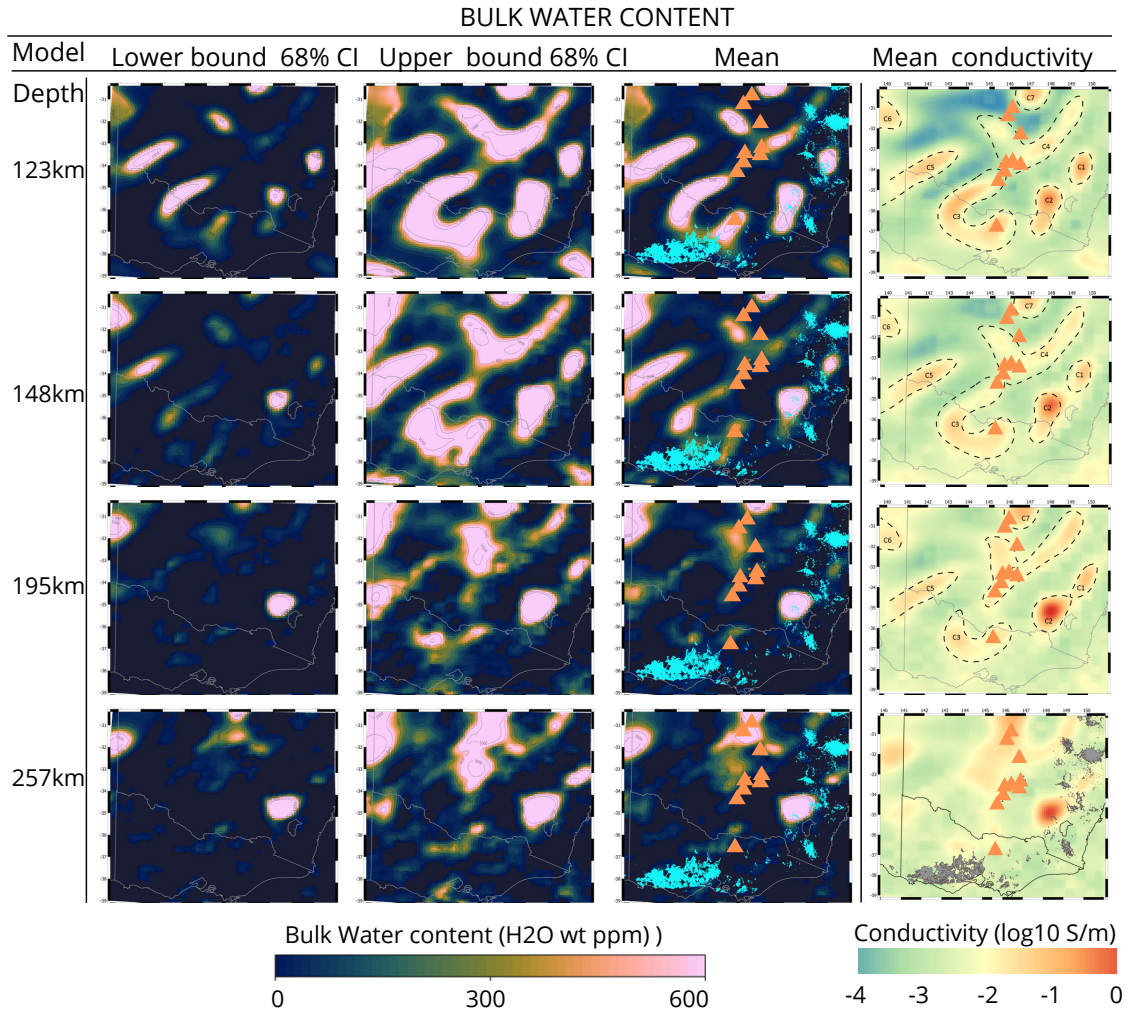


**Figure 14.** Bulk water content and mantle conductivity models from the joint probabilistic inversion. Columns (1)-(3): water content maps obtained from the (1) the lower, (2) upper bound of the 68% CI and (3) mean conductivity models. Column (4): depth slices from mean conductivity models of the posterior PDF. The location of leucitite-bearing volcanism and basaltic volcanoes are shown in orange and turquoise in (3); and orange and in grey in (4). We refer to the main text for an explanation of structures C1-C7. Selected depths are shown on the left of the figure.



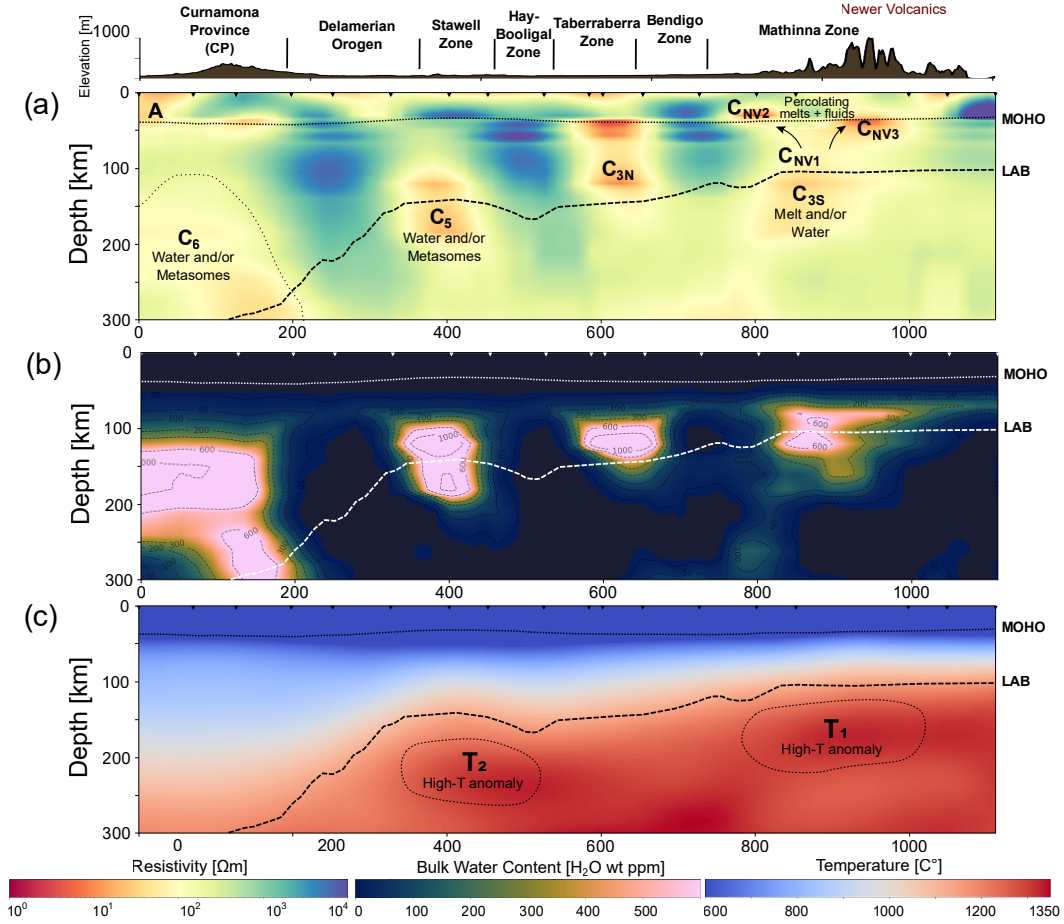


**Figure 15.** Vertical slices along transect A-A' (crossing most of the geological provinces) of a) the mean conductivity model, b) bulk water content derived from the mean conductivity mode and c) temperature. The Moho and LAB depths along that transect are shown in dashed lines in all panels. The elevation and location of the geological provinces is shown at the top of the figure.

513 The north-south transects in Figure 16 show a bulge and two defined steps in the  
 514 lithospheric structure at  $\sim 50$ ,  $\sim 300$  and  $\sim 650$  km close to where the northern and  
 515 central leucitites, and basaltic volcanoes erupted on the surface, respectively. These fea-  
 516 tures in the LAB correlate with the location of sub-lithospheric high-conductivity regions  
 517 ( $C_7$ ,  $C_4$  and  $C_{3S}$ ). Comparing the conductivity, bulk water, and thermal structure, we  
 518 observe that while the water content at  $C_7$  and  $C_4$  is likely to be large,  $C_{3S}$  correlates  
 519 with a semi-hydrated to dry mantle region. We also observe that the conductivity of  $C_{3S}$   
 520 can be explained by the high anomalous temperatures found in that region ( $T_1$ ).

521 Figures 17, with transects across the eastern basaltic volcanoes and the NV, show  
 522 the continuation of the structure  $C_{3S}$  beneath the NV. A high-conductivity and wet re-  
 523 gion ( $C_1$ ) is observed in the sub-lithospheric mantle below the Eastern Province. This  
 524 deep, wet structure is also seen in Figure S6 (Supplementary material) and correlates  
 525 with a high-temperature anomaly ( $T_3$ ). A discussion regarding the relationship between  
 526 water content, metasomatism and interpretation of the lithospheric structures described  
 527 in this section is given below.



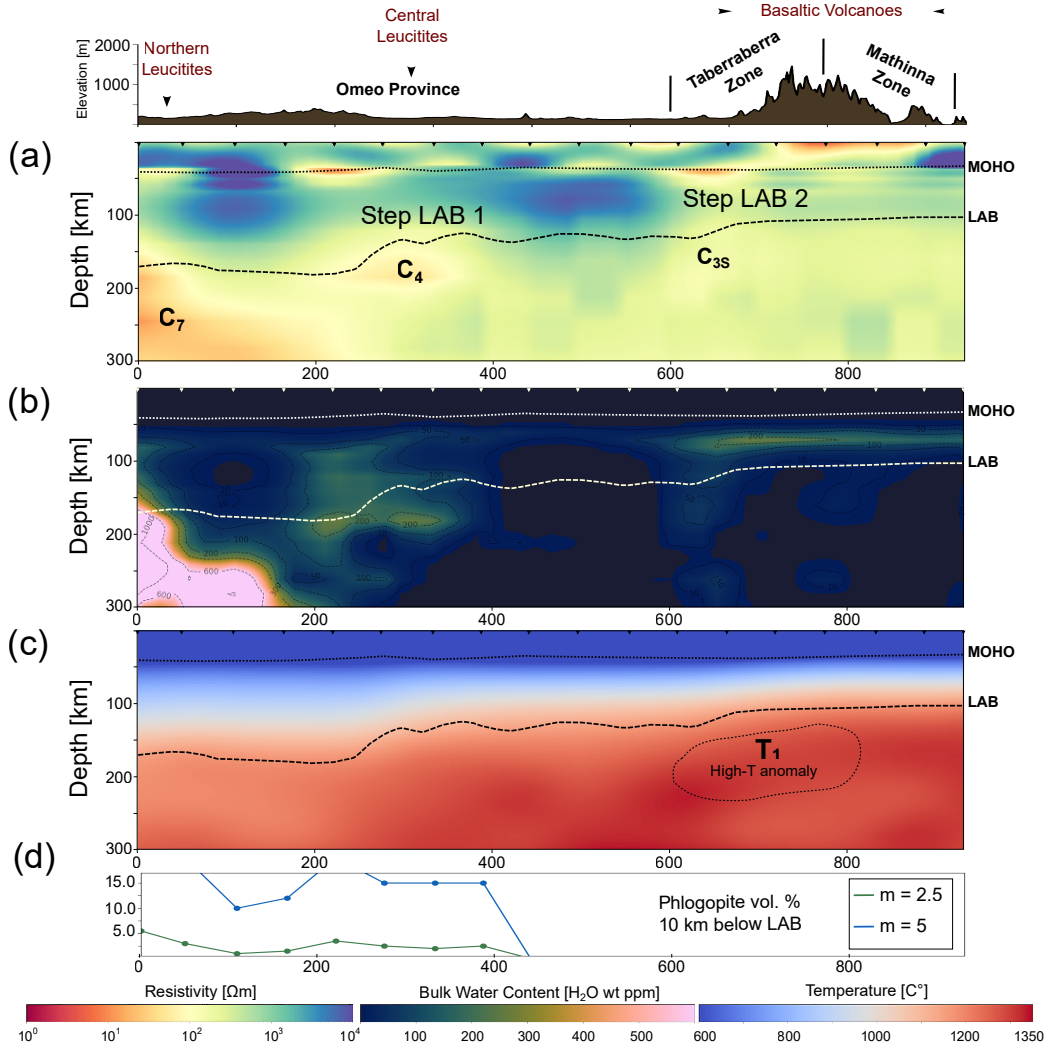


**Figure 16.** Vertical slices along transect D-A' (crossing the leucitite volcanics and basaltic volcanics in the south) of a) the mean conductivity model, b) bulk water content derived from the mean conductivity model and c) temperature. The Moho and LAB depths along that transect are shown in dashed lines in all panels. d) Intermediately connected ( $m=2.5$  in blue) and poorly connected ( $m=5$  in green) phlogopite in a dry lherzolitic matrix that fit the observed conductivities along the transect. The elevation and location of the volcanics and the NV are shown at the top of the figure.

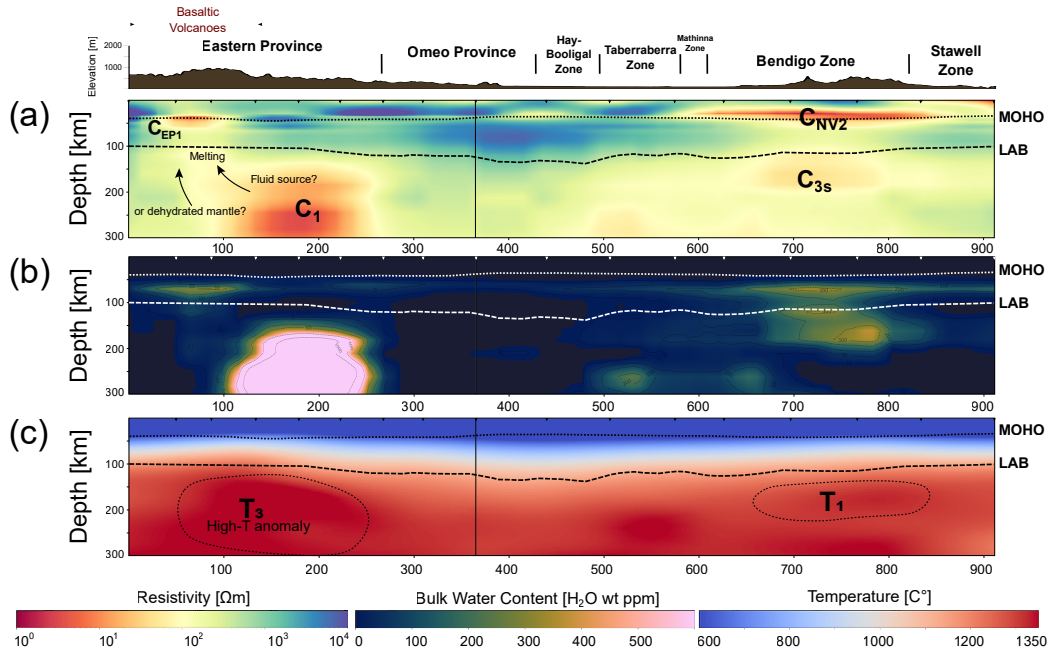


**Figure 17.** Vertical slices along transect B''-B'-B (across the basaltic volcanoes on the east and the NV) of a) the mean conductivity model, b) bulk water content derived from the mean conductivity model and c) temperature. The Moho and LAB depths along that transect are shown in dashed lines in all panels. The LAB depth along that transect is shown in dashed-black line in all panels. The elevation and location of the volcanics and the NV are shown at the top of the figure.

## 5 Discussion

### 5.1 Mantle metasomatism and lithospheric structure

Mantle metasomatism occurs when incipient melts or fluids react with mantle rocks. These reactions can impart chemical enrichments or alter the modal mineralogy of a mantle domain. The latter i) affect the modal proportions of peridotites, ii) introduce new volatile-bearing phases (phlogopite, amphibole, apatite, and carbonates) and, in some pervasive cases, iii) create new lithological domains, such as pyroxenite  $\pm$  volatile-bearing phase lithologies (e.g. O'Reilly & Griffin, 1987). The generation of volatile-bearing phases reduces the solidus temperature (Foley et al., 2009; Pintér et al., 2021a) and increases the electrical conductivity of the mantle domain (Selway, 2014).

The bulk water content we report in this study acts as a general proxy for metasomatism or mantle fertility, i.e., the inclusion of phases (metasomes) that increase the electrical conductivity of the mantle. This proxy indicates, for example, i) the presence of water and/or phases such as graphite or sulphides for depths above 75-120 km (Selway, 2014; Özaydın & Selway, 2020); ii) co-existing water and phlogopite in cold mantle below 75-120 km depth; or iii) presence of melt in regions of elevated temperatures (via the joint assessment of bulk water content and temperature models).

#### 5.1.1 Metasomatism across Tasmanides

Figures 15.a-b demonstrate consistent southeastward dipping lithospheric-scale structures from CP to Bendigo Zone, which correlate well with the limits of the geological provinces. We observe a successive alternation of conductive/wet and resistive/dry lithospheres that resemble the west-to-east subduction-accretion process in eastern Australia (Glen, 2005; Shea et al., 2022). The joint assessment of the transects in Figure 15 suggests that the hydrated and cold region  $C_6$  is likely subjected to pervasive mantle metasomatism. This result is consistent with the accretion process in the area, whereby successive subduction and orogenic events introduced material into the mantle to act as metasomatic agents and, overtime, preferentially metasomatized the old, thick lithosphere.

The crustal conductor (A) below CP (described in Section 4.3.1) can be seen in Figure 15a. Kay et al. (2022) interpreted this region as deposition of interconnected graphite, which either stems from a shallow/crustal biotic source from tectonic imbrication or an abiotic source related to ascending fluids from a metasomatized mantle. We observe that the deep metasomatized mantle below CP shown in our results provides evidence to explain an abiotic source for the shallow crustal conductors. Moreover, an abiotic source could provide the mantle source reservoir for the unique heavy  $\delta C^{13}$  eastern Australian Group B alluvial diamonds from the Wellington field and Bingara, New South Wales (Davies et al., 2002).

#### 5.1.2 Metasomatism below leucitite volcanoes

The leucitite lavas have melt compositions comparable to lamproites, and were derived from atypical mantle assemblage of phlogopite bearing pyroxenite (Shea et al., 2022). Due to these lava compositions, Kirkby et al. (2020) interpreted the conductors beneath the central leucitites as phlogopite stored in the mantle, suggesting a metasomatized and volatile-rich mantle region. Given the high conductivities ( $< 100\Omega$  m) and bulk water content ( $\sim 200$  ppm) observed around  $C_4$  (Figures 16), our results indicate a high probability for the presence of volatile-bearing minerals, likely introduced via modal mantle metasomatism.

Using the water calculation setup described in Section 3.5 and the phlogopite conductivity model of Li et al. (2017), we calculated the electrical conductivities of lherzolite with 5 and 10 % vol. of 0.52 w.t. fluorine-bearing phlogopite (average fluorine value

of mantle rocks, Özyayın et al., 2022) for both perfectly connected ( $m = 1.1$ , Modified Archie’s Law) and sparsely populated phlogopites ( $m = 6$ , Modified Archie’s Law). The results show that perfectly connected cases are 2.5 orders of magnitude more conductive than the observed conductivities in the region, while the conductivity for sparsely populated/disconnected cases lay near the lower bound of the observed conductivities (Figure S7). These results suggest that a lherzolite with 5-10 % vol of intermediately connected ( $6 < m < 1.1$ ) phlogopite explains the conductivities in  $C_4$ . Furthermore, leucite melting from a hydrous pyroxenite source could exhaust phlogopites in the assemblage (Foley et al., 2022). If past melts have destroyed phlogopites from the source region, the residue would be reminiscent of an enriched and hydrated lherzolite (Green, 2015). Since the water content for a residual hydrous lherzolite (Green, 2015) matches with the observed bulk water content in region  $C_4$ , we conclude that the most applicable explanation for the high conductivities observed in  $C_4$  is a hydrous lherzolite with small percentages of intermediately interconnected to sparsely populated phlogopite. These results are also illustrated in Figure 16.d, which shows the percentage of intermediately connected ( $m=2.5$ ) phlogopite that can explain the observed conductivities across the leucitites volcanoes. Since large volume of phlogopite would drastically lower the seismic velocities (e.g., Selway et al., 2015) and this is not seen in our models, we note that the large percentages ( $\geq 15\%$ ) of poorly connected ( $m=5$ ) phlogopites are unlikely to explain the conductivities in the region.

The northern leucitites sit above a high-conductivity and metasomatized region below the LAB ( $C_7$ ). The ultrapotassic compositions of these lavas suggest lower-degree partial melting (Cundari, 1973) which is consistent with the colder temperatures found in the region. Furthermore, potassium-rich magmas are produced by melting of a metasomatized mantle source that has been enriched in phlogopite (Xu et al., 2017; Förster et al., 2019). We calculated the effect of phlogopites in this region and found similar results to those for the central leucite (Figures 16.d and S6) favoring intermediately connected phlogopites. The higher conductivities and colder temperature in this region compared to the central leucitites provide a favorable scenario for the presence of existing phlogopites that survived previous melting events.

### 5.1.3 Metasomatism underneath Newer Volcanics

The lithospheric step at  $\sim 650$  km in Figures 16 sits below the basaltic volcanoes. This step is also seen in Figure 15 and correlates with the sub-lithospheric conductor  $C_{3S}$  and a high temperature anomaly of  $\sim 1350-1400^\circ C$  ( $T_1$ ). From the low-velocities observed at 60-80 km beneath the NV (Figure 5), Rawlinson et al. (2017) interpreted this temperature anomaly as a mantle upwelling and the source of the NV (see also Rawlinson et al., 2015). The existence of shallow mantle upwellings beneath lava field volcanism provides a favorable setting for decompression melting and mantle metasomatism (Aivazpourporgou et al., 2015).

In order to assess the existence of current melting in the region, we calculated water-depressed solidus curves (Hirschmann et al., 2009) for four cases of melt with the observed conductivities, temperatures and bulk water content in the lithospheric column beneath NV (Figure S8 in Supplementary Material). These four cases have melt mass fractions ( $\Phi$ ) and Generalised Archie’s Law cementation component ( $m$ ) of: (I)  $\Phi = 1\%$ ,  $m = 6$ ; (II)  $\Phi = 1\%$ ,  $m = 1.1$ ; (III)  $\Phi = 10\%$ ,  $m = 6$ ; (IV)  $\Phi = 10\%$ ,  $m = 6$ . For the calculations we used the melt electrical conductivity model of Sifré et al. (2014), water-partitioning coefficients between melt and minerals for garnets from Novella et al. (2014) and the coefficients from Hirschmann et al. (2009) for olivine and pyroxenes. The results indicate that the geotherm in the region is not hot enough to maintain melt generation with the water content observed at  $C_{3S}$  only. However, melt can be maintained through the assimilation of carbon-bearing species and an oxidised solidus (Pintér et al., 2021b). Carbonate-bearing xenoliths entrained in lavas from NV show strong evidence for carbonatite meta-

somatism in the source (Yaxley et al., 1991, 1998) and could indicate presence of melt and incipient metasomatic agents (Frey et al., 1978) in the region.

We interpret that conductive metasomatic agents that percolated from  $C_{3S}$  and then  $C_{NV1}$  are a feasible explanation for the high conductivity values observed in the conductors  $C_{NV2}$  and  $C_{NV3}$  found at  $\sim 20\text{--}75$  km depth beneath the basaltic volcanoes (Figure 15). This finding is consistent with the work of Shea et al. (2022) which shows that the compositions of these basalts cannot be produced by melting a garnet lherzolite mantle source, instead requiring modally metasomatized mantle sources of enriched mantle, likely pyroxenites  $\pm$  hydrous phases (Frey et al., 1978; O'Reilly & Zhang, 1995; Zhang et al., 2001; Zhang & O'Reilly, 1997). This interpretation is further supported by extensive sampling of metasomatized xenoliths, including carbonate-, phlogopite-, pargasite-, and apatite-bearing samples found throughout the Newer Volcanics (Frey & Green, 1974; Yaxley et al., 1991, 1998; Bonadiman et al., 2021; Lu et al., 2020).

#### 5.1.4 Metasomatism beneath Eastern basaltic volcanics

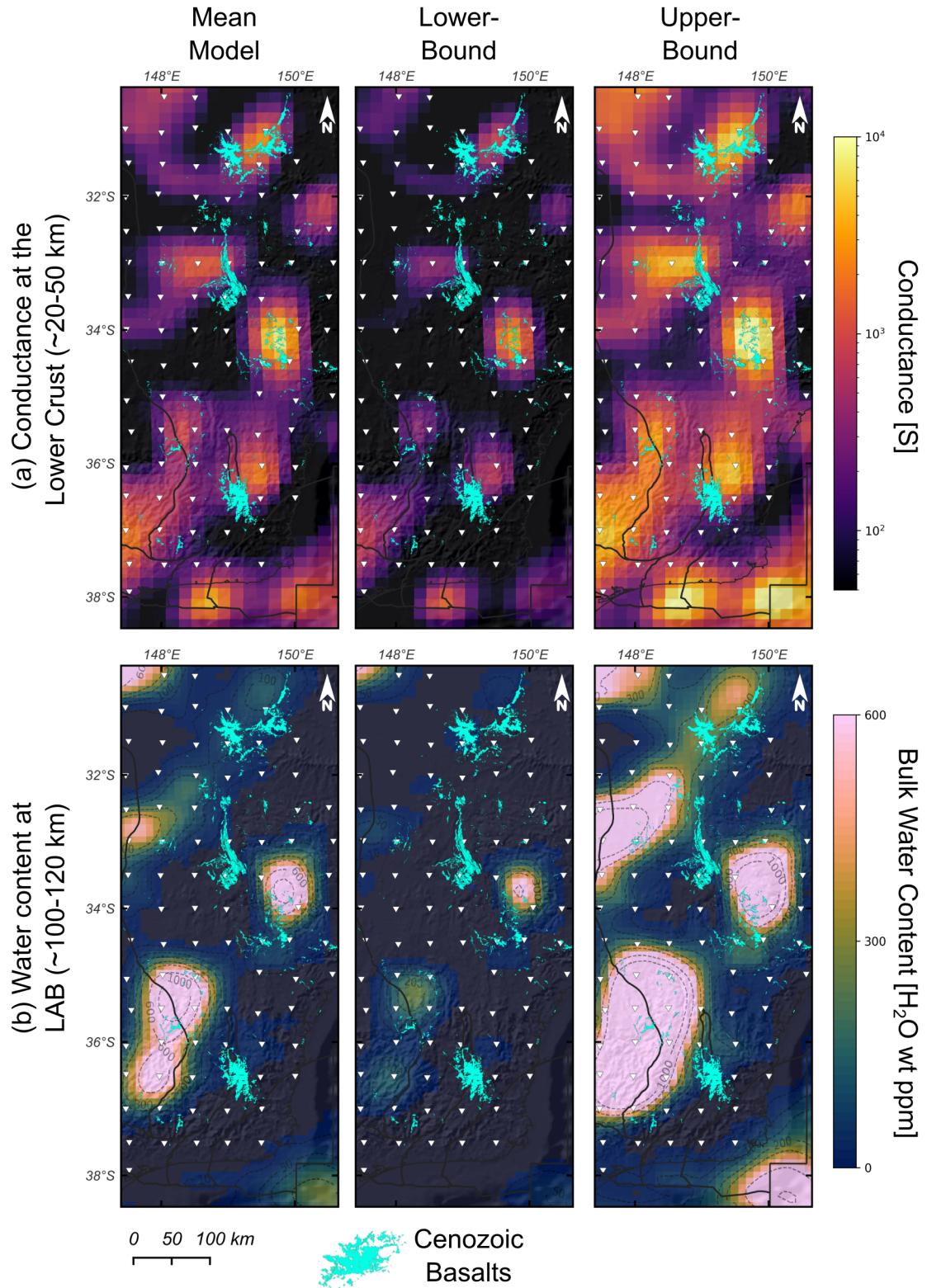
Beneath the volcanics of the Eastern Province, we observe highly-metasomatized sub-lithospheric regions ( $C_1$  and  $C_4$ ) and shallow conductors ( $C_{EP1}$ ,  $C_{EP2}$ ,  $C_{EP3}$ ) at  $\sim 50$  km depth (Figures 17 and S6). The conductor  $C_1$  correlates with a deep temperature anomaly  $T_3$  and a low-velocity anomaly (Figures 5). Rawlinson et al. (2015) has interpreted this velocity anomaly as the mantle source for the eastern basaltic volcanoes. Following the procedure describe above, we evaluate the existence of melt in this region (Figures S9) for melt mass fractions  $\Phi = 0.25\%$  and  $\Phi = 1\%$  using highly interconnected (Tubes model, Ten Grotenhuis et al., 2005) and unconnected (H-S bounds, Glover et al., 2000) melt models. The results indicate that the temperatures in  $T_3$  are not hot enough to maintain melt only with water in the system. However, the geotherm might be just hot enough to produce some percentage of melt in combination with water and carbon-reduced solidus. If melting exist, it could be low-degree volatile-rich incipient melts that are acting as metasomatic agents; which, may be producing metasomatized mantle domains to act as sources for future major melting events (Shea et al., 2022).

Figure 18 demonstrates the relationship between the location of volcanics in the Eastern Province, the distribution of shallow conductors (average conductance 20-50 km) and mantle metasomatism (through average water content near the LAB). According to these results, basalt fields tend to be associated with shallow conductors (Figure 18a) and a dryer lithosphere (Figure 18b). Basalts also tend to surround the most metasomatized/conductive regions of the lithosphere, similar to what has been observed with kimberlites worldwide (Özaydın & Selway, 2022). Furthermore, the clear association with the distribution of lavas and shallow conductors indicate that the lavas sourced from deep mantle and traversed towards the crust. On their ascend, the lavas precipitated conductive minerals forming shallow conductors ( $C_{EP1}$ ,  $C_{EP2}$ ,  $C_{EP3}$  in Figures 17 and S6). Figure 17 shows a clear conductive pathway from  $C_1$  to  $C_{EP1}$ , while the mantle beneath the volcanics is relatively dry. This dry mantle beneath the lava fields may indicate that the high-degree melting events may have exhausted the mantle source region in metasomes and water. Another possibility is that basaltic lavas were sourced from adjacent conductive/metasomatic mantle regions ( $C_1$  and  $C_4$ ) via oblique trans-lithospheric weakness zones. Further analysis with contributions from geodynamic modeling, seismic tomography and melt modeling may be required to understand the full-scope behind the genesis of melts and their structural control towards the surface in Eastern Australia.

## 5.2 Implications for magma generation beneath eastern Australia

Age-progressive volcanism in the EAVP, particularly along the Cosgrove track (Davies et al., 2015), has been widely attributed to mantle plume activity since Wellman & McDougall (1974). However, Shea et al. (2022) shows primitive melt compositions through-





**Figure 18.** Relationship between Cenozoic Basalts and the parameters derived from the electrical conductivity model: (a) Conductance of the lower-crust ( $\sim 20 - 50$  km), (b) water content calculated around the LAB depth ( $\sim 100 - 120$  km).

678 out the EAVP, including all age-progressive volcanism, can only be produced by melt-  
 679 ing metasomatized mantle source assemblages such as pyroxenites  $\pm$  hydrous phases (am-  
 680 phibole and phlogopite)  $\pm$  Ti-bearing oxides  $\pm$  apatite. These melt composition do not  
 681 show much, and in most cases no input, from peridotite assemblages, which argues that  
 682 melt generation temperatures are too low to be driven by mantle plume activity.

683 The solidi for metasomatized mantle assemblages are  $\sim 300^\circ\text{C}$  lower than anhy-  
 684 drous peridotites, due to their high volatile concentrations stored in hydrous minerals.  
 685 In this way, melting metasomatized assemblages can produce realistic melt fractions with  
 686 only slight perturbations above ambient upper mantle temperatures ( $\sim 1350^\circ\text{C}$ ). Fur-  
 687 thermore, the models of Duvernay et al. (2021a) show that shear-driven upwelling (SDU)  
 688 and edge-driven convection (EDC) processes that account for water content in the up-  
 689 per mantle at  $\sim 1350^\circ\text{C}$  can produce enough melt to explain the total melt volume in  
 690 the EAVP. This scenario combined with the imaged metasomatized mantle regions sug-  
 691 gest that EDC and SDU are the dominant melting mechanism in eastern Australia rather  
 692 than mantle plume activity (Davies & Rawlinson, 2014; Duvernay et al., 2021b; Shea et  
 693 al., 2022).

694 Our results show a series of steps in the LAB that correlate well with both the lo-  
 695 cation of basaltic and leucitites volcanoes (Figures 16 and 19). With the Australian litho-  
 696 spheric plate moving northeast, these steps constitute areas prone to generating sublitho-  
 697 spheric small-scale, EDC instabilities (e.g., Zlotnik et al., 2008; Van Wijk et al., 2010;  
 698 Davies & Rawlinson, 2014; Ballmer et al., 2011; Afonso et al., 2008). As illustrated in  
 699 Figure 19, due to the plate motion metasomatized lithologies from thick older lithosphere  
 700 adjacent to places where EDC occur ( $C_4$  and  $C_{3S}$ ) are detached and dragged into the  
 701 EDC-cell. This asthenospheric flow creates SDU and EDC where the metasomatic litholo-  
 702 gies melt contributing to primary intraplate magmas or metasomatized intraplate melt  
 703 source. This incipient melt can react with the overlying portion of the LAB to create  
 704 the source of these volcanoes.

705 If we think the EDC as a regenerative process and given the continuous displace-  
 706 ment of the Australian plate, the question that arises is why the EDC is not generat-  
 707 ing melt continuously? We argued that the metasomatism regions act as a fusible for melt  
 708 generation. Once the metasomatic lithologies (linked to the orogenic accretion) enter the  
 709 cell they deplete and the melt generation stops. The residual of this process (hydrous  
 710 phases) will most likely emplace in neighbouring regions. The importance of the conduc-  
 711 tivity and water content models obtained in the joint probabilistic inversion is that they  
 712 are imaging the residue of these interactions rather than the actual source of the Ceno-  
 713 zoic volcanoes. Since numerical simulations show that EDC are normally unstable and  
 714 transitory (REFS), small perturbations in the sub-lithospheric mantle such as sudden  
 715 acceleration of plate motion could produce new EDCs (REFS). The production of melt  
 716 is likely to start when the EDC develops close to “new” metasomatized region in the litho-  
 717 sphere.

## 718 6 Conclusions

719 The results presented here demonstrate the feasibility, benefits and performance  
 720 of our probabilistic approach for imaging the thermochemical structure of the lithosphere.  
 721 The joint probabilistic inversion of 3D magnetotellurics (MT) and seismic data helps un-  
 722 lock the full potential of the MT method by providing meaningful interpretations to the  
 723 conductivity anomalies and opens up new avenues for investigating metasomatism and  
 724 tectono-magmatic systems. In particular, our methodology:

- 725 • Succeeded in imaging electrical conductivity, seismic velocity, and temperature struc-  
 726 tures also identified by independent studies (Kirkby et al., 2020; Rawlinson et al.,

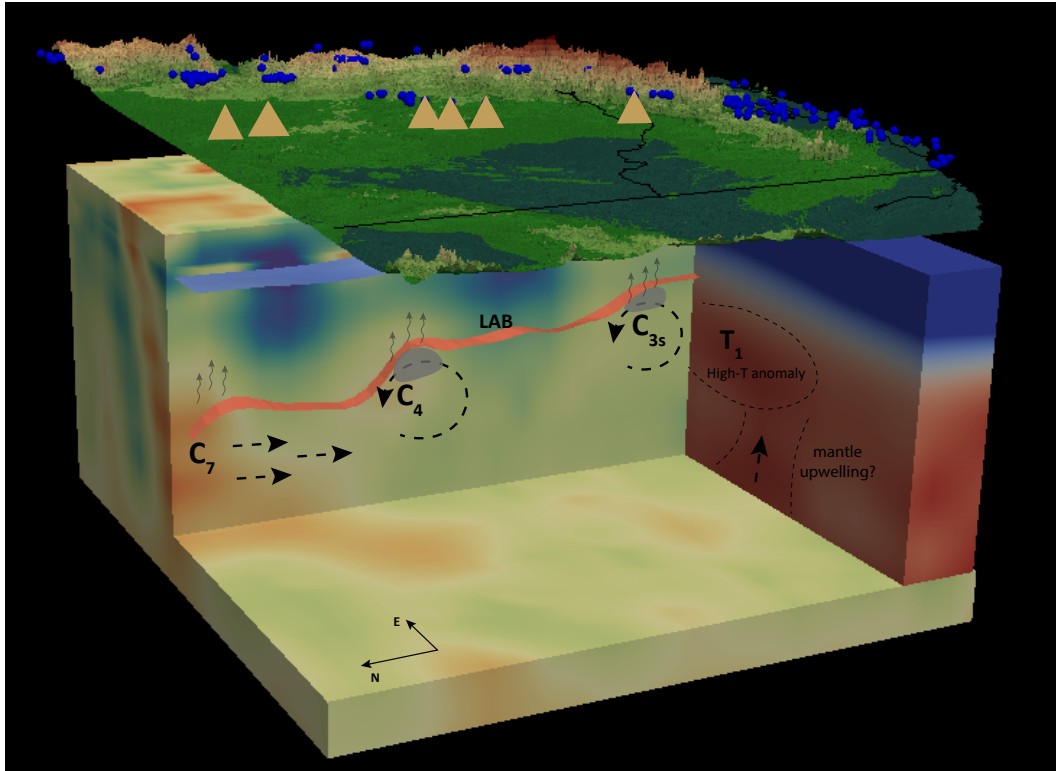


**Figure 19.** Interactions between mantle metasomatism and steps in the LAB. Dashed arrows show the flow of the asthenosphere and shearing of enriched mantle material into EDC-cells. Hotspots along the LAB are indicated by grey blobs, and locally occur where enriched mantle material crosses its solidus in the sub-lithospheric mantle. Incipient melts (grey arrows) may also travel along the LAB from deep to shallow portions of the lithospheric mantle.



2017; Davies et al., 2015; Pilia et al., 2015, cf.), gravity and magnetic data in the region (Nakamura & Milligan, 2015; Nakamura, 2016);

- Deals with the non-uniqueness of the MT problem and provides quantitative information on model uncertainties via well-behaved posterior distributions. This information is crucial for constraining the factors affecting the electrical conductivity. Depending the geological setting, the uncertainty in conductivity can be linked to uncertainties in temperature, partial melt or bulk water content.
- Offers an improved integrated model of the lithosphere beneath southeast Australia, which is compatible with both MT and seismic data as well as geochemical information from xenoliths. The results show improved resolution of the lithosphere-asthenospheric boundary depths and mantle electrical conductivities due to the favorable constraint of the seismic data to the thermal structure in the joint probabilistic inversion.

This study images a highly heterogeneous lithosphere beneath eastern Australia and provides insights for geodynamic and tectono-magmatic processes across multiple scales. The main takeaways that stem from our analysis can be summarised as:

- Widespread mantle metasomatism is identified throughout the region, suggesting complex interactions in the asthenosphere-lithosphere system.
- An alternation of conductive/wet and resistive/dry lithospheres that correlates with the location of geological provinces, resembling the west-to-east subduction-accretion process in eastern Australia.
- Associations between the lithospheric structure, metasomatized regions and distribution of magmatism within the Eastern Australian Volcanic Province (EAVP) are observed. For instance, high correlations are seen between the metasomatized mantle and the location of leucitite and basaltic volcanic centers. The high conductivities observed below the leucitite volcanoes indicate a residual hydrous lherzolite with small percentages of intermediately interconnected to sparsely populated phlogopite.
- The conductivities and temperature found beneath the Newer Volcanics suggest that melt maintained through the assimilation of carbon-bearing phases can exist in the region. This interpretation is supported by samples of metasomatized xenoliths throughout the EAVP.
- A series of steps in the present-day thermal structure correlate with the location of volcanic centers and constitute areas prone to develop small-scale edge-driven convection (EDC) cells in the sub-lithospheric mantle. These results, together with the petrology and melt chemistry presented in Shea et al. (2022), suggest that localised EDC processes are likely to account for the volcanism along the age-progressive tracks in EAVP, rather than a hot mantle plume (Davies et al., 2015; Kirkby et al., 2020).

## Appendix A Sampling Strategy

The sampling strategy is specifically tailored to take advantage of the differential sensitivities of the seismic and MT data sets to the background and anomalous structures of the lithosphere (see Manassero et al., 2021). With this in mind, we subdivided the MCMC simulation into three main searches. The first search uses the column-based parameterization only to constrain the background conductivity and seismic velocities associated with the first-order temperature structure and large thermal anomalies. At each MCMC step, new models are obtained by randomly choosing a column and sampling all the column-parameters from their proposal distributions (Gaussian distributions centered in the current sample). The prior for the LABs are uniform distributions defined in a wide range ( $60 < LAB < 320$  km) to include most of the variability that

777 exists in continental settings (e.g. Griffin et al., 2009; Pasyanos, 2010; Fishwick, 2010;  
 778 Hasterok & Chapman, 2011; Afonso et al., 2013a, and references therein). The same type  
 779 of distributions are used for the thermal nodes and  $V_P$  velocities in crustal layers with  
 780 bounds  $400\text{--}1600^\circ\text{C}$  and  $2\text{--}6.5\text{ km/s}$ , respectively. The second search focuses on con-  
 781 straining the conductivity anomalies that do not depend on thermo-physical state by sam-  
 782 pling the conductivity nodes while still allowing the sampling of the column-parameters.  
 783 At each MCMC iteration, the algorithm randomly chooses a type of parameter to sam-  
 784 ple (i.e. column or nodes). If a column is selected, the sampling strategy corresponds  
 785 to that of the first search, otherwise the algorithm randomly chooses  $n$  nodes at a time  
 786 and assigns a conductivity value from its proposal distribution (log-normal distributions).  
 787 The prior for the conductivity nodes are Gaussian distributions centered on the back-  
 788 ground conductivity value (in log-scale) and standard deviation  $2 \log_{10}(S/m)$ . This range  
 789 is large enough to keep the search as general as possible and to include most of the anoma-  
 790 lous conductivity over the background. For a new set of nodes' values, only the 3D con-  
 791 ductivity model is updated via interpolation using kriging (Appendix C) and its likeli-  
 792 hood is only evaluated with the 3D MT forward solution. After these stages, the pro-  
 793 posal distributions are adapted to multi-dimensional Gaussian and log-normal distribu-  
 794 tions for the column-parameters and the node-parameters, respectively, via the AM al-  
 795 gorithm. At each MCMC step of the this third stage, a *metropolized independence sam-*  
 796 *pler* randomly selects to sample  $N_{col}$  columns or  $N_{nodes}$  nodes.

797 Using prior information from previous inversions in eastern Australia, the initial  
 798 3D model (i.e., starting point) of our MCMC simulation is constructed by assembling  
 799 the LAB depths for each 1D column from the model of Rawlinson et al. (2017) The crustal  
 800 layers' RHP are obtained with a previous 1D joint probabilistic inversion (Haynes et al.,  
 801 2020; Afonso et al., 2013a, 2013b). The initial  $V_P$  for the crustal layers and Moho depths  
 802 (Figure 1.e) are taken from the regional AusREM model (Australian Seismological Ref-  
 803 erence Earth Model, Kennett & Salmon, 2012) and the initial value for each thermal node  
 804 is derived from an adiabat between the initial LAB and the node at 410 km depth ( $T_{410} =$   
 805  $1500^\circ\text{C}$ ). For the conductivity nodes, the initial values are computed as two orders of mag-  
 806 nitude more resistive than the conductivity value at the nodes' location given by a pre-  
 807 vious deterministic inversion (Kirkby et al., 2020). In this work, we ran a total of 2,500,000  
 808 s MCMC steps for 15 frequencies using 2 processors(Intel(R) Xeon(R) CPU E5-2680 v3  
 809 @ 2.50GHz) per frequency. Even with modest computational resources, the inversion took  
 810 61 days with an average of 2.64 s per simulation. This represents a time reduction of  $\sim$   
 811 94% in the computation of the forward solution for this model.

## 812 **Appendix B Mapping Thermochemical Parameters to Background Elec-** 813 **trical Conductivity**

The background conductivity structure is parameterized using the depth to the LAB and temperature nodes placed in the sub-lithospheric upper mantle. For this, we first discretized the 3D numerical model in  $M_{col}$  columns. Each column is made up of  $n_x \times n_y \times n_z$  FE cells (forward problem discretization) and it is characterized by its own LAB depth, temperature nodes, bulk mantle composition and radioactive heat production (RHP) in the crust. The LAB depth and RHP are used to compute a lithospheric thermal profile by solving the 1D steady-state finite-element heat transfer problem in each column (Afonso, Rawlinson, et al., 2016) with Dirichlet boundary conditions at the surface ( $T_0 = 10^\circ\text{C}$ ) and at each LAB depth ( $T_{LAB} = 1250^\circ\text{C}$ ) (cf. Afonso, Moorkamp, & Fulla, 2016). We also compute a thermal profile in the asthenosphere interpolating the temperature-nodes from the LAB to the bottom of the numerical domain (410 km) and a pressure profile in the whole model using the following quadratic lithostatic-type approximation and the density in the crust:

$$P(z) = 0.99 \times (4.4773 \times 10^{-3}z^2 + 3.2206 \times 10^4z - 1.284278 \times 10^8) \quad (\text{B1})$$

814 where  $P$  is pressure in  $Pa$  and  $z$  is depth in meters.

Table B1: Parameters used to compute mantle conductivity

Phase	$\sigma_0$	$\sigma_{0i}$	a	b	c	d	e	f	$\Delta V$	$\Delta H_i$
Olivine	2.70	4.73	1.64	0.246	-4.85	3.26			0.68	2.31
Opx	3.0		1.90	-2.77	2.61	-1.09				
Cpx	3.25		2.07	-2.77	2.61	-1.09				
Garnet		4.96	2.60	-15.33	80.40	-194.6	202.6	-75.0		

815 At each FE cell, we obtain the mineral phases in vol% and iron content ( $X_{Fe}$ ) for  
816 olivine, orthopyroxene, clinopyroxene and garnet as a function of temperature and pres-  
817 sure in the mantle from pre-computed tables. These tables contain equilibrium assem-  
818 blages and associated thermophysical properties derived by free energy minimization (Afonso  
819 et al., 2013b) for different temperature, pressures and major-oxide compositions. The  
820 electrical conductivity for each mineral phase is obtained using the following Arrhenius-  
821 type equation with parameters specified in Table B1:

$$\sigma = \sigma_0 \exp\left(\frac{-\Delta H(X_{Fe}, P)}{k_B T}\right) + \sigma_{0i} \exp\left(\frac{-\Delta H_i}{k_B T}\right) + \sigma_p \quad (\text{B2a})$$

$$\sigma_p = f(C_w) \exp\left(\frac{-\Delta H_{wet}(C_w)}{k_B T}\right), \quad (\text{B2b})$$

$$-\Delta H(X_{Fe}, P) = a + bX_{Fe} + cX_{Fe}^2 + dX_{Fe}^3 + eX_{Fe}^4 + fX_{Fe}^5 + P\Delta V, \quad (\text{B2c})$$

822 where  $\sigma_0$ ,  $\sigma_{0i}$  [S/m] and  $f(C_w)$  are the small polaron, ionic and proton pre-exponential  
823 factors, respectively,  $\Delta V$  [cm<sup>3</sup>/mol] is the activation volume,  $\Delta H$ ,  $\Delta H_i$  [eV] and  $\Delta H_{wet}$   
824 are activation enthalpies and  $X_{Fe}$  is the bulk Fe content in wt%.

825 The first term in the right-hand side of Equation B2a describes the contribution  
826 from small polaron conduction. Its activation enthalpy depends on iron content and pres-  
827 sure and its represented by a polynomial on  $X_{Fe}$  (Eq. B2c) plus a term that depends  
828 on pressure (the coefficients  $a, b, c, d, e, f$  are determined experimentally). The user can  
829 choose to consider the effect of the iron content in olivine and orthopyroxene or not. The  
830 second term of Equation B2a represents ionic conduction at high temperature and the  
831 third term ( $\sigma_p$ ) represents the proton conduction due to hydrogen diffusion.  $f(C_w)$  and  
832  $\Delta H_{wet}$  are functions of the water content  $C_w$  [wt%] and they are obtained from labo-  
833 ratory experiments (see e.g., Pommier, 2014; Jones, 2014, 2016). In this study we in-  
834 clude the proton conduction term of Gardés et al. (2014b) for olivine and the term based  
835 on Dai & Karato (2009b) for pyroxenes. However, in scenarios where the mantle com-  
836 position is barely known, we choose to work with a dry mantle and let the conductiv-  
837 ity nodes accommodate the effect of water content. The preferred model for small po-  
838 laron of dry garnet is based on Dai & Karato (2009d) whereas the iron effect is taken  
839 from Romano et al. (2006). The parameters for small polaron and ionic conduction for  
840 olivine, orthopyroxene clinopyroxene and garnet used in our inversion are summarised  
841 in Table A1. Finally, the bulk electrical conductivity corresponding to each FE cell is  
842 computed using the lower bound of the Hashin–Shtrikman averaging scheme (Hashin  
843 & Shtrikman, 1962, 1963).

## Appendix C Conductivity Nodes to Anomalous Electrical Conductivity

The conductivity structures related with smaller-scale features in the crust and over the background are parameterized with 7648 nodes sparsely located within the entire 3D volume. In order to define the location of the nodes, the numerical domain is first subdivided into horizontal layers (every two FE cells in the vertical direction) where their mid-points correspond to the vertical location of the nodes. Considering that bodies with dimensions smaller than the electromagnetic skin depth cannot be resolved by the MT data, the horizontal distance between nodes within each layer is chosen relative to the skin depth for the range of periods and apparent resistivities shown in the observed data. The nodal values are interpolated to each FE cell of the numerical domain via kriging (Gaussian process) interpolation (see e.g. Cressie, 1993; Rasmussen, 1997; Williams & Rasmussen, 1996; Omre, 1987; Gibbs & MacKay, 1997; Gibbs, 1998). The main idea of this method to predict the value of a function  $Z$  at  $m$  locations from  $n$  observations by computing average spatial weights ( $W$ ). In simple kriging, these weights are derived using a known covariance function  $c$  between observations (given by the matrix  $K_{obs}$ ) and between the observations and the  $m$  estimation locations (given by the covariance matrix  $K_{loc}$ ):

$$W = K_{obs}^{-1} \cdot K_{loc}, \quad (C1)$$

$$\text{where } K_{obs} = \begin{pmatrix} c(x_1^{obs}, x_1^{obs}) & \dots & c(x_1^{obs}, x_n^{obs}) \\ \dots & \dots & \dots \\ c(x_n^{obs}, x_1^{obs}) & \dots & c(x_n^{obs}, x_n^{obs}) \end{pmatrix} \text{ and } K_{loc} = \begin{pmatrix} c(x_1^{obs}, x_1^{loc}) & \dots & c(x_1^{obs}, x_m^{loc}) \\ \dots & \dots & \dots \\ c(x_n^{obs}, x_1^{loc}) & \dots & c(x_n^{obs}, x_m^{loc}) \end{pmatrix}.$$

The interpolation (or estimated value) at the  $m$  locations is then given by  $Z^{loc} = W \cdot Z^{obs}$ , where  $Z^{obs}$  is the vector containing the  $n$  observations. We use a positive definite covariance function with spatially variable correlation lengths (Gibbs & MacKay, 1997; Gibbs, 1998; Manassero et al., 2021):

$$c(\mathbf{x}_m, \mathbf{x}_n) = \theta_1 \prod_l \left( \frac{2r_l(\mathbf{x}_m)r_l(\mathbf{x}_n)}{r_l^2(\mathbf{x}_m) + r_l^2(\mathbf{x}_n)} \right)^{1/2} \exp\left( - \sum_l \frac{(x_m^l - x_n^l)^2}{r_l^2(\mathbf{x}_m) + r_l^2(\mathbf{x}_n)} \right) \quad (C2)$$

where  $r_l(\mathbf{x})$  is an arbitrary parameterized function of position  $\mathbf{x}$  defined in  $[-1, 1]^2 \times [0, 1]$ . The form of  $r_l(\mathbf{x})$  as a function of the scaled coordinates  $(x, y, z)$  used in the main text is shown in Procedure 1 in Supplementary Material.

### Acknowledgments

The data is available at [github.com/manassero/Joint\\_Inv\\_SEAUS/tree/main/DATA](https://github.com/manassero/Joint_Inv_SEAUS/tree/main/DATA). We kindly thank Nicholas Rawlinson and Simone Pilia for providing the seismic velocities models, and Anqi Zhang for providing interpolation subroutines. We also thank Isra Ezad for her insightful comments. MCM thanks support from an International Macquarie Research Excellence Scholarship (iMQRES). MCM and JCA acknowledge support from ARC Grant DP160103502, ARC Linkage Grant LP170100233, the ARC Centre of Excellence Core to Crust Fluids Systems (<http://www.cafs.mq.edu.au>) and the center for Earth Evolution and Dynamics, Geoscience Australia and the European Space Agency via the “3D Earth - A Dynamic Living Planet”. SÖ thanks the support from the Macquarie University COVID Recovery Fellowship fund and JJS was funded through ARC grant FL180100134. ST publishes with the permission of the Director of the Geological Survey of South Australia. AK and KC acknowledge the teams from GA, GSNSW, GSV, GSSA and the University of Adelaide involved in collecting the data and the support provided by individuals and communities to access the country, especially in remote and rural Australia. AK



870 and KR publish with the permission of the CEO, Geoscience Australia. Resources from  
871 Macquarie University were used for this work.

## 872 References

- 873 Afonso, J. C., Fullea, J., Griffin, W., Yang, Y., Jones, A., Connolly, J., & O'Reilly,  
874 S. (2013a). 3-D multiobservable probabilistic inversion for the compositional and  
875 thermal structure of the lithosphere and upper mantle. I: A priori petrological  
876 information and geophysical observables. *Journal of Geophysical Research: Solid*  
877 *Earth*, *118*(5), 2586–2617.
- 878 Afonso, J. C., Fullea, J., Yang, Y., Connolly, J., & Jones, A. (2013b). 3-D multi-  
879 observable probabilistic inversion for the compositional and thermal structure of  
880 the lithosphere and upper mantle. II: General methodology and resolution analy-  
881 sis. *Journal of Geophysical Research: Solid Earth*, *118*(4), 1650–1676.
- 882 Afonso, J. C., Moorkamp, M., & Fullea, J. (2016). Imaging the lithosphere and  
883 upper mantle: Where we are at and where we are going. In N. L. M. Moorkamp  
884 P. Lelievre & A. Khan (Eds.), *Integrated imaging of the earth: Theory and appli-*  
885 *cations* (pp. 191–218). John Wiley & Sons.
- 886 Afonso, J. C., Rawlinson, N., Yang, Y., Schutt, D. L., Jones, A. G., Fullea, J., &  
887 Griffin, W. L. (2016). 3-D multiobservable probabilistic inversion for the com-  
888 positional and thermal structure of the lithosphere and upper mantle: III. Ther-  
889 mochemical tomography in the Western-Central US. *Journal of Geophysical*  
890 *Research: Solid Earth*, *121*(10), 7337–7370.
- 891 Afonso, J. C., Zlotnik, S., & Fernandez, M. (2008). Effects of compositional and rhe-  
892 ological stratifications on small-scale convection under the oceans: Implications for  
893 the thickness of oceanic lithosphere and seafloor flattening. *Geophysical Research*  
894 *Letters*, *35*(20).
- 895 Aivazpourpogou, S., Thiel, S., Hayman, P. C., Moresi, L. N., & Heinson, G. (2015).  
896 Decompression melting driving intraplate volcanism in Australia: Evidence from  
897 magnetotelluric sounding. *Geophysical Research Letters*, *42*(2), 346–354.
- 898 Avdeeva, A., Moorkamp, M., Avdeev, D., Jegen, M., & Miensopust, M. (2015).  
899 Three-dimensional inversion of magnetotelluric impedance tensor data and full  
900 distortion matrix. *Geophysical Journal International*, *202*(1), 464–481.
- 901 Ballmer, M. D., Ito, G., Van Hunen, J., & Tackley, P. J. (2011). Spatial and tem-  
902 poral variability in Hawaiian hotspot volcanism induced by small-scale convection.  
903 *Nature Geoscience*, *4*(7), 457–460.
- 904 Bedrosian, P. A. (2016). Making it and breaking it in the Midwest: Continental  
905 assembly and rifting from modeling of EarthScope magnetotelluric data. *Precam-*  
906 *brian Research*, *278*, 337–361.
- 907 Bell, D. R., Ihinger, P. D., & Rossman, G. R. (1995). Quantitative analysis of trace  
908 oh in garnet and pyroxenes. *American Mineralogist*, *80*(5-6), 465–474.
- 909 Bennington, N. L., Zhang, H., Thurber, C. H., & Bedrosian, P. A. (2015). Joint  
910 inversion of seismic and magnetotelluric data in the Parkfield Region of California  
911 using the normalized cross-gradient constraint. *Pure and Applied Geophysics*,  
912 *172*(5), 1033–1052.
- 913 Birch, W. D. (1978). Mineralogy and geochemistry of the leucitite at cosgrove, victo-  
914 ria. *Journal of the Geological Society of Australia*, *25*(7-8), 369–385.
- 915 Blackburn, G., Allison, G. B., & Leaney, F. W. J. (1982). Further evidence on the  
916 age of the tuff at mt gambier, south australia. *Transactions of the Royal Society of*  
917 *South Australia*, *106*, 163–167. Retrieved from [https://archive.org/details/](https://archive.org/details/TransactionsRoy106Roya/mode/2up)  
918 [TransactionsRoy106Roya/mode/2up](https://archive.org/details/TransactionsRoy106Roya/mode/2up)
- 919 Blatter, D., Naif, S., Key, K., & Ray, A. (2022). A plume origin for hydrous melt at  
920 the lithosphere–asthenosphere boundary. *Nature*, *604*(7906), 491–494.
- 921 Bonadiman, C., Brombin, V., Andreozzi, P., G. and Benna, Coltorti, M., Curetti, N.,

- 922 Faccini, B., . . . Stagno, V. (2021). Phlogopite-pargasite coexistence in an oxygen  
 923 reduced spinel-peridotite ambient. *Scientific Reports*, *11*(1), 1–17.
- 924 Boyd, F. (1989a). Compositional distinction between oceanic and cratonic litho-  
 925 sphere. *Earth and Planetary Science Letters*, *96*(1-2), 15–26.
- 926 Boyd, F. (1989b, 12). Compositional distinction between oceanic and cratonic  
 927 lithosphere. *Earth and Planetary Science Letters*, *96*, 15–26. Retrieved from  
 928 <https://linkinghub.elsevier.com/retrieve/pii/0012821X89901209> doi:  
 929 10.1016/0012-821X(89)90120-9
- 930 Brocher, T. M. (2005). Empirical relations between elastic wavespeeds and density  
 931 in the Earth’s crust. *Bulletin of the seismological Society of America*, *95*(6), 2081–  
 932 2092.
- 933 Cayley, R. (2011). Exotic crustal block accretion to the eastern Gondwanaland  
 934 margin in the Late Cambrian-Tasmania, the Selwyn Block, and implications for  
 935 the Cambrian-Silurian evolution of the Ross, Delamerian, and Lachlan orogens.  
 936 *Gondwana Research*, *19*(3), 628–649.
- 937 Cayley, R., & Musgrave, R. (2015). The Giant Lachlan Orocline—a powerful new  
 938 predictive tool for mineral exploration under cover across eastern Australia. *Mines  
 939 & Wines*, 29–38.
- 940 Champion, D. C., Brown, C., Mathews, E., Huston, D. L., & Kositsin, N. (2016).  
 941 *Geodynamic synthesis of the Phanerozoic of eastern Australia*. Geoscience Aus-  
 942 tralia.
- 943 Chave, A. D., & Jones, A. G. (2012). *The magnetotelluric method: Theory and prac-  
 944 tice*. Cambridge University Press.
- 945 Cline Ii, C., Faul, U., David, E., Berry, A., & Jackson, I. (2018). Redox-influenced  
 946 seismic properties of upper-mantle olivine. *Nature*, *555*(7696), 355–358.
- 947 Cohen, B. E., Mark, D. F., Fallon, S. J., & Stephenson, P. J. (2017, 4). Holocene-  
 948 neogene volcanism in northeastern australia: Chronology and eruption his-  
 949 tory. *Quaternary Geochronology*, *39*, 79–91. Retrieved from [https://  
 950 www.sciencedirect.com/science/article/pii/S1871101416300826](https://www.sciencedirect.com/science/article/pii/S1871101416300826) doi:  
 951 10.1016/J.QUAGEO.2017.01.003
- 952 Comeau, M. J., Unsworth, M. J., Ticona, F., & Sunagua, M. (2015). Magnetotelluric  
 953 images of magma distribution beneath Volcán Uturuncu, Bolivia: Implications for  
 954 magma dynamics. *Geology*, *43*(3), 243–246.
- 955 Connolly, J. (2009). The geodynamic equation of state: what and how. *Geochem-  
 956 istry, Geophysics, Geosystems*, *10*(10).
- 957 Cordell, D., Naif, S., Troch, J., & Huber, C. (2022). Constraining magma reservoir  
 958 conditions by integrating thermodynamic petrological models and bulk resis-  
 959 tivity from magnetotellurics. *Geochemistry, Geophysics, Geosystems*, *23*(9),  
 960 e2022GC010455.
- 961 Cressie, N. (1993). *Statistics for spatial data* (Revised Edition ed.). Wiley-  
 962 Interscience.
- 963 Cundari, A. (1973). Petrology of the leucite-bearing lavas in New South  
 964 Wales. *Journal of the Geological Society of Australia*, *20*, 465–492. Re-  
 965 trieved from <https://doi.org/10.1080/00167617308728829> doi: 10.1080/  
 966 00167617308728829
- 967 Dai, L., & Karato, S.-i. (2009a). Electrical conductivity of orthopyroxene: Im-  
 968 plications for the water content of the asthenosphere. *Proceedings of the Japan  
 969 Academy, Series B*, *85*(10), 466–475.
- 970 Dai, L., & Karato, S.-i. (2009b). Electrical conductivity of orthopyroxene: Im-  
 971 plications for the water content of the asthenosphere. *Proceedings of the Japan  
 972 Academy, Series B*, *85*(10), 466–475.
- 973 Dai, L., & Karato, S.-i. (2009c). Electrical conductivity of pyrope-rich garnet at  
 974 high temperature and high pressure. *Physics of the Earth and Planetary Interiors*,  
 975 *176*(1-2), 83–88.

- 976 Dai, L., & Karato, S.-i. (2009d). Electrical conductivity of pyrope-rich garnet at  
 977 high temperature and high pressure. *Physics of the Earth and Planetary Interiors*,  
 978 *176*(1-2), 83–88.
- 979 Davies, O'Reilly, S., & Griffin, W. (2002). Multiple origins of alluvial diamonds from  
 980 New South Wales, Australia. *Economic Geology*, *97*(1), 109–123.
- 981 Davies, & Rawlinson, N. (2014). On the origin of recent intraplate volcanism in Aus-  
 982 tralia. *Geology*, *42*(12), 1031–1034.
- 983 Davies, Rawlinson, N., Iaffaldano, G., & Campbell, I. H. (2015). Lithospheric con-  
 984 trols on magma composition along Earth's longest continental hotspot track. *Nature*,  
 985 *525*(7570), 511–514.
- 986 Demidjuk, Z., Turner, S., Sandiford, M., George, R., Foden, J., & Etheridge, M.  
 987 (2007). U-series isotope and geodynamic constraints on mantle melting processes  
 988 beneath the Newer Volcanic Province in South Australia. *Earth and Planetary*  
 989 *Science Letters*, *261*(3-4), 517–533.
- 990 Demouchy, S., Shcheka, S., Denis, C. M., & Thoraval, C. (2017). Subsolidus hy-  
 991 drogen partitioning between nominally anhydrous minerals in garnet-bearing  
 992 peridotite. *American Mineralogist: Journal of Earth and Planetary Materials*,  
 993 *102*(9), 1822–1831.
- 994 Duvernay, T., Davies, D. R., Mathews, C., Gibson, A., & Kramer, S. (2021b). Link-  
 995 ing intraplate volcanism to lithospheric structure and asthenospheric flow. *Geo-*  
 996 *chemistry, Geophysics, Geosystems*, *22*, 1-29. doi: 10.1029/2021GC009953
- 997 Duvernay, T., Davies, D. R., Mathews, C. R., Gibson, A. H., & Kramer, S. C.  
 998 (2021a). Linking intraplate volcanism to lithospheric structure and asthenospheric  
 999 flow. *Geochemistry, Geophysics, Geosystems*, *22*(8), e2021GC009953.
- 1000 Evans, R. (2012). Conductivity of Earth materials. In J. A. Chave A. (Ed.), *The*  
 1001 *magnetotelluric method, theory and practice* (pp. 50–95). Cambridge: Cambridge  
 1002 Univ. Press New York.
- 1003 Evans, R., Benoit, M. H., Long, M. D., Elsenbeck, J., Ford, H. A., Zhu, J., & Gar-  
 1004 cia, X. (2019). Thin lithosphere beneath the central Appalachian Mountains: A  
 1005 combined seismic and magnetotelluric study. *Earth and Planetary Science Letters*,  
 1006 *519*, 308–316.
- 1007 Farquharson, C. G., & Oldenburg, D. W. (1998). Non-linear inversion using general  
 1008 measures of data misfit and model structure. *Geophysical Journal International*,  
 1009 *134*(1), 213–227.
- 1010 Fishwick, S. (2010). Surface wave tomography: imaging of the lithosphere–  
 1011 asthenosphere boundary beneath central and southern Africa? *Lithos*, *120*(1-2),  
 1012 63–73.
- 1013 Foley, S., Ezad, I., van der Laan Sieger, & Pertermann, M. (2022, 3). Melting of  
 1014 hydrous pyroxenites with alkali amphiboles in the continental mantle: 1. melt-  
 1015 ing relations and major element compositions of melts. *Geoscience Frontiers*,  
 1016 101380. Retrieved from [https://linkinghub.elsevier.com/retrieve/pii/](https://linkinghub.elsevier.com/retrieve/pii/S1674987122000330)  
 1017 [S1674987122000330](https://linkinghub.elsevier.com/retrieve/pii/S1674987122000330) doi: 10.1016/j.gsf.2022.101380
- 1018 Foley, S., Yaxley, G., Rosenthal, A., Buhre, S., Kiseeva, E., Rapp, R., & Jacob, D.  
 1019 (2009). The composition of near-solidus melts of peridotite in the presence of CO<sub>2</sub>  
 1020 and H<sub>2</sub>O between 40 and 60 kbar. *Lithos*, *112*, 274–283.
- 1021 Förster, M. W., Buhre, S., Xu, B., Prelević, D., Mertz-Kraus, R., & Foley, S. F.  
 1022 (2019). Two-stage origin of k-enrichment in ultrapotassic magmatism simulated  
 1023 by melting of experimentally metasomatized mantle. *Minerals*, *10*(1), 41.
- 1024 Frey, F., & Green, D. (1974). The mineralogy, geochemistry and origin of iherzo-  
 1025 lite inclusions in victorian basanites. *Geochimica et Cosmochimica Acta*, *38*, 1023-  
 1026 1059. Retrieved from [http://www.sciencedirect.com/science/article/pii/](http://www.sciencedirect.com/science/article/pii/0016703774900039)  
 1027 [0016703774900039](http://www.sciencedirect.com/science/article/pii/0016703774900039) doi: [https://doi.org/10.1016/0016-7037\(74\)90003-9](https://doi.org/10.1016/0016-7037(74)90003-9)
- 1028 Frey, F., Green, D., & Roy, S. (1978). Integrated models of basalt petrogenesis: a  
 1029 study of quartz tholeiites to olivine melilitites from south eastern Australia utiliz-

- 1030 ing geochemical and experimental petrological data. *Journal of petrology*, 19(3),  
1031 463–513.
- 1032 Fullea, J., Muller, M., & Jones, A. (2011). Electrical conductivity of conti-  
1033 nental lithospheric mantle from integrated geophysical and petrological mod-  
1034 eling: Application to the Kaapvaal Craton and Rehoboth Terrane, southern  
1035 Africa. *Journal of Geophysical Research: Solid Earth*, 116(B10), 94–105. doi:  
1036 doi:10.1029/2011JB008544
- 1037 Gallardo, L. A., & Meju, M. A. (2007). Joint two-dimensional cross-gradient imag-  
1038 ing of magnetotelluric and seismic travelttime data for structural and lithological  
1039 classification. *Geophysical Journal International*, 169(3), 1261–1272.
- 1040 García-Yeguas, A., Ledo, J., Piña-Varas, P., Prudencio, J., Queralt, P., Marcuello,  
1041 A., . . . Pérez, N. (2017). A 3d joint interpretation of magnetotelluric and seismic  
1042 tomographic models: The case of the volcanic island of Tenerife. *Computers &  
1043 Geosciences*, 109, 95–105.
- 1044 Gardés, E., Gaillard, F., & Tarits, P. (2014a). Toward a unified hydrous olivine  
1045 electrical conductivity law. *Geochemistry, Geophysics, Geosystems*, 15(12), 4984–  
1046 5000.
- 1047 Gardés, E., Gaillard, F., & Tarits, P. (2014b). Toward a unified hydrous olivine  
1048 electrical conductivity law. *Geochemistry, Geophysics, Geosystems*, 15(12), 4984–  
1049 5000.
- 1050 Gibbs, M. (1998). *Bayesian Gaussian processes for regression and classification* (Un-  
1051 published doctoral dissertation). Citeseer.
- 1052 Gibbs, M., & MacKay, D. J. (1997). Efficient implementation of Gaussian processes.  
1053 *Neural Computation*.
- 1054 Gilks, W. R., Richardson, S., & Spiegelhalter, D. (1995). *Markov chain Monte Carlo  
1055 in practice*. Chapman and Hall/CRC.
- 1056 Glen, R. (2005). The tasmanides of eastern australia. *Special Publication-Geological  
1057 Society of London*, 246, 23.
- 1058 Glen, R. (2013). Refining accretionary orogen models for the Tasmanides of eastern  
1059 Australia. *Australian Journal of Earth Sciences*, 60(3), 315–370.
- 1060 Glover, P. W. (2010). A generalized archie’s law for n phases. *Geophysics*, 75(6),  
1061 E247–E265.
- 1062 Glover, P. W., Hole, M. J., & Pous, J. (2000). A modified Archie’s law for two con-  
1063 ducting phases. *Earth and Planetary Science Letters*, 180(3-4), 369–383.
- 1064 Goes, S., Govers, R., Vacher, & P. (2000). Shallow mantle temperatures under  
1065 Europe from P and S wave tomography. *Journal of Geophysical Research: Solid  
1066 Earth*, 105(B5), 11153–11169.
- 1067 Green, D. H. (2015). Experimental petrology of peridotites, including effects of wa-  
1068 ter and carbon on melting in the earth’s upper mantle. *Physics and Chemistry of  
1069 Minerals*, 42, 95–122. doi: 10.1007/s00269-014-0729-2
- 1070 Gregory, P. (2005). *Bayesian Logical Data Analysis for the Physical Sciences: A  
1071 Comparative Approach with Mathematica® Support*. Cambridge University Press.
- 1072 Griffin, W., Begg, G., & O’reilly, S. Y. (2013). Continental-root control on the gene-  
1073 sis of magmatic ore deposits. *Nature Geoscience*, 6(11), 905.
- 1074 Griffin, W., O’reilly, S. Y., Afonso, J. C., & Begg, G. (2009). The composition and  
1075 evolution of lithospheric mantle: a re-evaluation and its tectonic implications.  
1076 *Journal of Petrology*, 50(7), 1185–1204.
- 1077 Griffin, W., Sutherland, F., & Hollis, J. (1987, 4). Geothermal profile and crust-  
1078 mantle transition beneath east-central Queensland: Volcanology, xenolith petrol-  
1079 ogy and seismic data. *Journal of Volcanology and Geothermal Research*, 31,  
1080 177–203. Retrieved from [https://www.sciencedirect.com/science/article/  
1081 pii/0377027387900679](https://www.sciencedirect.com/science/article/pii/0377027387900679) doi: 10.1016/0377-0273(87)90067-9
- 1082 Haario, H., Laine, M., Mira, A., & Saksman, E. (2006). DRAM: efficient adaptive  
1083 MCMC. *Statistics and computing*, 16(4), 339–354.



- 1084 Hand, M. P., Reid, A. J., Szpunar, M. A., Direen, N., Wade, B., Payne, J., &  
 1085 Barovich, K. M. (2008). Crustal architecture during the early Mesoproterozoic  
 1086 Hiltaba-related mineralisation event: are the Gawler Range Volcanics a foreland  
 1087 basin fill? *MESA Journal*, *51*, 19–24.
- 1088 Hashin, Z., & Shtrikman, S. (1962). A variational approach to the theory of the ef-  
 1089 fective magnetic permeability of multiphase materials. *Journal of applied Physics*,  
 1090 *33*(10), 3125–3131.
- 1091 Hashin, Z., & Shtrikman, S. (1963). A variational approach to the theory of the  
 1092 elastic behaviour of multiphase materials. *Journal of the Mechanics and Physics*  
 1093 *of Solids*, *11*(2), 127–140.
- 1094 Hassani, B., & Renaudin, A. (2013). The cascade bayesian approach for a controlled  
 1095 integration of internal data, external data and scenarios.
- 1096 Hasterok, D., & Chapman, D. (2011). Heat production and geotherms for the conti-  
 1097 nental lithosphere. *Earth and Planetary Science Letters*, *307*(1-2), 59–70.
- 1098 Haynes, M., Fomin, I., Afonso, J. C., Gorbatov, A., Czarnota, K., & Salajegheh, F.  
 1099 (2020). *Developing thermochemical models of Australia’s lithosphere*. Geoscience  
 1100 Australia.
- 1101 Heinson, G., Didana, Y., Soeffky, P., Thiel, S., & Wise, T. (2018). The crustal  
 1102 geophysical signature of a world-class magmatic mineral system. *Scientific reports*,  
 1103 *8*(1), 1–6.
- 1104 Heinson, G., Duan, J., Kirkby, A., Robertson, K., Thiel, S., Aivazpourpogou, S., &  
 1105 Soyer, W. (2021). Lower crustal resistivity signature of an orogenic gold system.  
 1106 *Scientific Reports*, *11*(1), 1–7.
- 1107 Hirschmann, M. M., Tenner, T., Aubaud, C., & Withers, A. (2009). Dehydration  
 1108 melting of nominally anhydrous mantle: The primacy of partitioning. *Physics of*  
 1109 *the Earth and Planetary Interiors*, *176*(1-2), 54–68.
- 1110 Irving, A. J. (1980). Petrology and geochemistry of composite ultramafic xeno-  
 1111 liths in alkalic basalts and implications for magmatic processes within the mantle.  
 1112 *American Journal of Science*, *280*, 389–416.
- 1113 Jegen, M. D., Hobbs, R. W., Tarits, P., & Chave, A. (2009). Joint inversion of  
 1114 marine magnetotelluric and gravity data incorporating seismic constraints: Pre-  
 1115 liminary results of sub-basalt imaging off the Faroe Shelf. *Earth and Planetary*  
 1116 *Science Letters*, *282*(1-4), 47–55.
- 1117 Johnson, R. W., Johnson, R. W., Knutson, J., & Taylor, S. R. (1989). *Intraplate vol-*  
 1118 *canism: in eastern Australia and New Zealand*. Cambridge University Press.
- 1119 Jones, A. G. (1999). Imaging the continental upper mantle using electromagnetic  
 1120 methods. *Lithos*, *48*(1-4), 57–80.
- 1121 Jones, A. G. (2011). Three-dimensional galvanic distortion of three-dimensional  
 1122 regional conductivity structures: Comment on” three-dimensional joint inversion  
 1123 for magnetotelluric resistivity and static shift distributions in complex media” by  
 1124 Yutaka Sasaki and Max A. Meju. *Journal of Geophysical Research. Solid Earth*,  
 1125 *116*(12).
- 1126 Jones, A. G. (2014). Reconciling different equations for proton conduction using the  
 1127 Meyer-Neldel compensation rule. *Geochemistry, Geophysics, Geosystems*, *15*(2),  
 1128 337–349.
- 1129 Jones, A. G. (2016). Proton conduction and hydrogen diffusion in olivine: an at-  
 1130 tempt to reconcile laboratory and field observations and implications for the role  
 1131 of grain boundary diffusion in enhancing conductivity. *Physics and Chemistry of*  
 1132 *Minerals*, *43*(4), 237–265.
- 1133 Jones, A. G., Afonso, J. C., & Fullea, J. (2017). Geochemical and geophysical  
 1134 constrains on the dynamic topography of the Southern African Plateau. *Geochem-*  
 1135 *istry, Geophysics, Geosystems*, *18*(10), 3556–3575.
- 1136 Karato, S.-i. (1990). The role of hydrogen in the electrical conductivity of the upper  
 1137 mantle. *Nature*, *347*(6290), 272.

- 1138 Karato, S.-i. (2006). Remote sensing of hydrogen in earth’s mantle. *Reviews in Min-*  
 1139 *eralogy and Geochemistry*, 62(1), 343–375.
- 1140 Kay, B., Heinson, G., & Brand, K. (2022). Crustal magnetotelluric imaging of a Pa-  
 1141 leoproterozoic graphitic suture zone, Curnamona Province, Australia. *Gondwana*  
 1142 *Research*, 106, 1–14.
- 1143 Kelbert, A., Meqbel, N., Egbert, G. D., & Tandon, K. (2014). ModEM: A mod-  
 1144 ular system for inversion of electromagnetic geophysical data. *Computers & Geo-*  
 1145 *sciences*, 66, 40–53.
- 1146 Kennett, B., & Salmon, M. (2012). Ausrem: Australian seismological reference  
 1147 model. *Australian Journal of Earth Sciences*, 59(8), 1091–1103.
- 1148 Khan, A. (2016). On Earth’s mantle constitution and structure from joint analy-  
 1149 sis of geophysical and laboratory-based data: An example. *Surveys in Geophysics*,  
 1150 37(1), 149–189.
- 1151 Khan, A., Connolly, J., & Olsen, N. (2006). Constraining the composition and ther-  
 1152 mal state of the mantle beneath Europe from inversion of long-period electromag-  
 1153 netic sounding data. *Journal of Geophysical Research: Solid Earth*, 111(B10).
- 1154 Kirkby, A., Czarnota, K., Huston, D. L., Champion, D. C., Doublier, M. P.,  
 1155 Bedrosian, P. A., ... Heinson, G. (2022). Lithospheric conductors reveal source  
 1156 regions of convergent margin mineral systems. *Scientific Reports*, 12(1), 1–10.
- 1157 Kirkby, A., Musgrave, R. J., Czarnota, K., Doublier, M. P., Duan, J., Cayley, R. A.,  
 1158 & Kyi, D. (2020). Lithospheric architecture of a Phanerozoic orogen from mag-  
 1159 netotellurics: AusLAMP in the Tasmanides, southeast Australia. *Tectonophysics*,  
 1160 793, 228560.
- 1161 Li, Y., Jiang, H., & Yang, X. (2017). Fluorine follows water: Effect on electrical  
 1162 conductivity of silicate minerals by experimental constraints from phlogopite.  
 1163 *Geochimica et Cosmochimica Acta*, 217, 16–27.
- 1164 Liu, H., Zhu, Q., & Yang, X. (2019). Electrical conductivity of oh-bearing omphacite  
 1165 and garnet in eclogite: the quantitative dependence on water content. *Contribu-*  
 1166 *tions to Mineralogy and Petrology*, 174(7), 1–15.
- 1167 Lu, J., Griffin, W. L., Tilhac, R., Xiong, Q., Zheng, J., & O’Reilly, S. Y. (2018).  
 1168 Tracking deep lithospheric events with garnet-websterite xenoliths from southeast-  
 1169 ern Australia. *Journal of Petrology*, 59(5), 901–930.
- 1170 Lu, J., Tilhac, R., Griffin, W. L., Zheng, J., Xiong, Q., Oliveira, B., & O’Reilly,  
 1171 S. Y. (2020). Lithospheric memory of subduction in mantle pyroxenite xenoliths  
 1172 from rift-related basalts. *Earth and Planetary Science Letters*, 544, 116365.
- 1173 Manassero, M. C., Afonso, J. C., Zyserman, F., Jones, A., Zlotnik, S., & Fomin,  
 1174 I. (2021). A Reduced Order Approach for Probabilistic Inversions of 3D Mag-  
 1175 netotelluric Data II: Joint Inversion of MT and Surface-Wave Data. *Journal of*  
 1176 *Geophysical Research: Solid Earth*, 126(12), e2021JB021962.
- 1177 Manassero, M. C., Afonso, J. C., Zyserman, F., Zlotnik, S., & Fomin, I. (2020). A  
 1178 Reduced Order Approach for Probabilistic Inversions of 3D Magnetotelluric Data  
 1179 I: General Formulation. *Geophysical Journal International*, 223(3), 1837–1863.
- 1180 McDonough, W. (1990, 11). Constraints on the composition of the continental litho-  
 1181 spheric mantle. *Earth and Planetary Science Letters*, 101, 1-18. Retrieved from  
 1182 <https://linkinghub.elsevier.com/retrieve/pii/0012821X9090119I> doi: 10  
 1183 .1016/0012-821X(90)90119-I
- 1184 Miensopust, M. P., Queralt, P., Jones, A. G., & modellers, D. M. (2013). Mag-  
 1185 netotelluric 3-D inversion—a review of two successful workshops on forward and  
 1186 inversion code testing and comparison. *Geophysical Journal International*, 193(3),  
 1187 1216–1238.
- 1188 Moorkamp, M., Jones, A., & Eaton, D. (2007). Joint inversion of teleseismic re-  
 1189 ceiver functions and magnetotelluric data using a genetic algorithm: Are seismic  
 1190 velocities and electrical conductivities compatible? *Geophysical Research Letters*,  
 1191 34(16).

- 1192 Moorkamp, M., Jones, A., & Fishwick, S. (2010). Joint inversion of receiver func-  
 1193 tions, surface wave dispersion, and magnetotelluric data. *Journal of Geophysical*  
 1194 *Research: Solid Earth*, *115*(B4).
- 1195 Moresi, L., Betts, P. G., Miller, M. S., & Cayley, R. A. (2014). Dynamics of conti-  
 1196 nental accretion. *Nature*, *508*(7495), 245–248.
- 1197 Musgrave, R. (2015). Oroclines in the Tasmanides. *Journal of Structural Geology*,  
 1198 *80*, 72–98.
- 1199 Musgrave, R., & Rawlinson, N. (2010). Linking the upper crust to the upper mantle:  
 1200 comparison of teleseismic tomography with long-wavelength features of the gravity  
 1201 and magnetic fields of southeastern Australia. *Exploration Geophysics*, *41*(2),  
 1202 155–162.
- 1203 Naif, S., Selway, K., Murphy, B. S., Egbert, G., & Pommier, A. (2021). Electric-  
 1204 al conductivity of the lithosphere-asthenosphere system. *Physics of the Earth and*  
 1205 *Planetary Interiors*, *313*(2021), 10661.
- 1206 Nakamura, A. (2016). *Isostatic residual gravity anomaly grid of onshore Australia*  
 1207 *2016*.
- 1208 Nakamura, A., & Milligan, P. (2015). *Total magnetic intensity (TMI) colour compos-*  
 1209 *ite image. Canberra: Geoscience Australia*.
- 1210 Novella, D., Frost, D. J., Hauri, E. H., Bureau, H., Raepsaet, C., & Roberge, M.  
 1211 (2014). The distribution of h<sub>2</sub>o between silicate melt and nominally anhydrous  
 1212 peridotite and the onset of hydrous melting in the deep upper mantle. *Earth and*  
 1213 *Planetary Science Letters*, *400*, 1–13.
- 1214 Omre, H. (1987). Bayesian kriging—merging observations and qualified guesses in  
 1215 kriging. *Mathematical Geology*, *19*(1), 25–39.
- 1216 O’Reilly, S., & Griffin, W. (1985, 1). A xenolith-derived geotherm for southeastern  
 1217 australia and its geophysical implications. *Tectonophysics*, *111*, 41–63. Retrieved  
 1218 from <https://linkinghub.elsevier.com/retrieve/pii/0040195185900654>  
 1219 doi: 10.1016/0040-1951(85)90065-4
- 1220 O’Reilly, S., & Griffin, W. (1987). Eastern Australia-4000 kilometres of mantle sam-  
 1221 ples. In *Mantle xenoliths* (pp. 267–280). John Wiley & Sons.
- 1222 Özyaydın, S., & Selway, K. (2020). MATE: An analysis tool for the interpretation  
 1223 of magnetotelluric models of the mantle. *Geochemistry, Geophysics, Geosystems*,  
 1224 *21*(9), e2020GC009126.
- 1225 Özyaydın, S., & Selway, K. (2022). The relationship between kimberlitic magmatism  
 1226 and electrical conductivity anomalies in the mantle. *Geophysical Research Letters*,  
 1227 e2022GL099661.
- 1228 Özyaydın, S., Selway, K., Griffin, W. L., & Moorkamp, M. (2022). Probing the south-  
 1229 ern African lithosphere with magnetotellurics: 2. Linking electrical conductivity,  
 1230 composition, and tectonomagmatic evolution. *Journal of Geophysical Research:*  
 1231 *Solid Earth*, *127*(3), e2021JB023105.
- 1232 O’Reilly, S. Y., & Zhang, M. (1995). Geochemical characteristics of lava-field basalts  
 1233 from eastern Australia and inferred sources: connections with the subcontinental  
 1234 lithospheric mantle? *Contributions to Mineralogy and Petrology*, *121*(2), 148–170.
- 1235 Padrón-Navarta, J. A., & Hermann, J. (2017). A subsolidus olivine water solubil-  
 1236 ity equation for the earth’s upper mantle. *Journal of Geophysical Research: Solid*  
 1237 *Earth*, *122*(12), 9862–9880.
- 1238 Page, R., Conon, C., Stevens, B., Gibson, G. M., Preiss, W. V., & Southgate, P.  
 1239 (2005). Correlation of Olary and Broken Hill domains, Curnamona Province:  
 1240 Possible relationship to Mount Isa and other North Australian Pb-Zn-Ag-bearing  
 1241 successions. *Economic Geology*, *100*(4), 663–676.
- 1242 Pasyanos, M. E. (2010). Lithospheric thickness modeled from long-period surface  
 1243 wave dispersion. *Tectonophysics*, *481*(1–4), 38–50.
- 1244 Pearson, N., O’Reilly, S., & Griffin, W. (1991, 6). Heterogeneity in the thermal state  
 1245 of the lower crust and upper mantle beneath eastern australia. *Exploration Geo-*

- 1246 *physics*, 22, 295–298. Retrieved from [https://www.tandfonline.com/doi/full/](https://www.tandfonline.com/doi/full/10.1071/EG991295)  
 1247 10.1071/EG991295 doi: 10.1071/EG991295
- 1248 Pilia, S., Rawlinson, N., Cayley, R., Bodin, T., Musgrave, R., Reading, A., ...  
 1249 Young, M. (2015). Evidence of micro-continent entrainment during crustal ac-  
 1250 cretion. *Scientific reports*, 5(1), 1–6.
- 1251 Pintér, Z., Foley, S. F., Yaxley, G. M., Rosenthal, A., Rapp, R. P., Lanati, A. W., &  
 1252 Rushmer, T. (2021a). Experimental investigation of the composition of incipient  
 1253 melts in upper mantle peridotites in the presence of CO<sub>2</sub> and H<sub>2</sub>O. *Lithos*, 396,  
 1254 106224.
- 1255 Pintér, Z., Foley, S. F., Yaxley, G. M., Rosenthal, A., Rapp, R. P., Lanati, A. W., &  
 1256 Rushmer, T. (2021b). Experimental investigation of the composition of incipient  
 1257 melts in upper mantle peridotites in the presence of co<sub>2</sub> and h<sub>2</sub>o. *Lithos*, 396,  
 1258 106224.
- 1259 Pommier, A. (2014). Interpretation of magnetotelluric results using laboratory mea-  
 1260 surements. *Surveys in Geophysics*, 35(1), 41–84.
- 1261 Rasmussen, C. E. (1997). *Evaluation of Gaussian processes and other methods for*  
 1262 *non-linear regression* (Unpublished doctoral dissertation). University of Toronto  
 1263 Toronto, Canada.
- 1264 Rawlinson, N., Davies, D., & Pilia, S. (2017). The mechanisms underpinning Ceno-  
 1265 zoic intraplate volcanism in eastern Australia: Insights from seismic tomography  
 1266 and geodynamic modeling. *Geophysical Research Letters*, 44(19), 9681–9690.
- 1267 Rawlinson, N., Kennett, B., Salmon, M., & Glen, R. (2015). Origin of lateral  
 1268 heterogeneities in the upper mantle beneath south-east Australia from seismic  
 1269 tomography. In *The earth's heterogeneous mantle* (pp. 47–78). Springer.
- 1270 Rawlinson, N., Pilia, S., Young, M., Salmon, M., & Yang, Y. (2016). Crust and  
 1271 upper mantle structure beneath southeast Australia from ambient noise and tele-  
 1272 seismic tomography. *Tectonophysics*, 689, 143–156.
- 1273 Raymond, O., Liu, S., Gallagher, R., Zhang, W., & Highet, L. (2012). Surface ge-  
 1274 ology of Australia 1: 1 million scale dataset 2012 edition. *Geoscience Australia*,  
 1275 *Canberra*.
- 1276 Raymond, O., Totterdell, J., Stewart, A., & Woods, M. (2018). Australian Geologi-  
 1277 cal Provinces, 2018. *Geoscience Australia, Canberra*.
- 1278 Ringwood, A. E. (1962, 2). A model for the upper mantle. *Journal of Geophysical*  
 1279 *Research*, 67, 857–867. doi: 10.1029/JZ067i002p00857
- 1280 Robertson, K., Heinson, G., & Thiel, S. (2016). Lithospheric reworking at the  
 1281 Proterozoic–Phanerozoic transition of Australia imaged using AusLAMP Magne-  
 1282 totelluric data. *Earth and Planetary Science Letters*, 452, 27–35.
- 1283 Romano, C., Poe, B. T., Kreidie, N., & McCammon, C. A. (2006). Electrical con-  
 1284 ductivities of pyrope–almandine garnets up to 19 GPa and 1700 C. *American Min-  
 1285 eralogist*, 91(8-9), 1371–1377.
- 1286 Rosas-Carbajal, M., Linde, N., Kalscheuer, T., & Vrugt, J. A. (2013). Two-  
 1287 dimensional probabilistic inversion of plane-wave electromagnetic data: methodol-  
 1288 ogy, model constraints and joint inversion with electrical resistivity data. *Geophys-  
 1289 ical Journal International*, 196(3), 1508–1524.
- 1290 Rosenbaum, G. (2018). The Tasmanides: Phanerozoic tectonic evolution of eastern  
 1291 Australia. *Annual Review of Earth and Planetary Sciences*, 46, 291–325.
- 1292 Selway, K. (2014). On the causes of electrical conductivity anomalies in tectonically  
 1293 stable lithosphere. *Surveys in Geophysics*, 35(1), 219–257.
- 1294 Selway, K., Ford, H., & Kelemen, P. (2015). The seismic mid-lithosphere discontinu-  
 1295 ity. *Earth and Planetary Science Letters*, 414, 45–57.
- 1296 Selway, K., & O’Donnell, J. (2019). A small, unextractable melt fraction as the  
 1297 cause for the low velocity zone. *Earth and Planetary Science Letters*, 517, 117–  
 1298 124.
- 1299 Shea, J. J., Ezad, I. S., Foley, S. F., & Lanati, A. W. (2022, 8). The eastern aus-

- 1300 tralian volcanic province, its primitive melts, constraints on melt sources and the  
 1301 influence of mantle metasomatism. *Earth-Science Reviews*, 104168. Retrieved from  
 1302 <https://linkinghub.elsevier.com/retrieve/pii/S0012825222002525> doi:  
 1303 10.1016/j.earscirev.2022.104168
- 1304 Sifré, D., Gardés, E., Massuyeau, M., Hashim, L., Hier-Majumder, S., & Gail-  
 1305 lard, F. (2014, May). Electrical conductivity during incipient melting in the  
 1306 oceanic low-velocity zone. *Nature*, 509(7498), 81–85. Retrieved 2022-04-27, from  
 1307 <http://www.nature.com/articles/nature13245> doi: 10.1038/nature13245
- 1308 Smith, B. W., & Prescott, J. R. (1987). Thermoluminescence dating of the eruption  
 1309 at mt schank, south australia. *Australian Journal of Earth Sciences*, 34, 335-342.  
 1310 doi: 10.1080/08120098708729415
- 1311 Snyder, D., Hillier, M., Kjarsgaard, B., De Kemp, E., & Craven, J. (2014). Litho-  
 1312 spheric architecture of the Slave craton, northwest Canada, as determined from  
 1313 an interdisciplinary 3-D model. *Geochemistry, Geophysics, Geosystems*, 15(5),  
 1314 1895–1910.
- 1315 Stixrude, L., & Lithgow-Bertelloni, C. (2011). Thermodynamics of mantle minerals-  
 1316 ii. phase equilibria. *Geophysical Journal International*, 184(3), 1180–1213.
- 1317 Sutherland, F., Graham, I., Meffre, S., Zwingmann, H., & Pogson, R. (2012).  
 1318 Passive-margin prolonged volcanism, East Australian Plate: outbursts, progres-  
 1319 sions, plate controls and suggested causes. *Australian Journal of Earth Sciences*,  
 1320 59(7), 983–1005.
- 1321 Sutherland, F., Raynor, L., & Pogson, R. (1994). Spinel to garnet lherzolite transi-  
 1322 tion in relation to high temperature palaeogeotherms, eastern australia. *Australian*  
 1323 *Journal of Earth Sciences*, 41, 205-220. doi: 10.1080/08120099408728130
- 1324 Takam Takougang, E. M., Harris, B., Kepic, A., & Le, C. V. (2015). Cooperative  
 1325 joint inversion of 3D seismic and magnetotelluric data: With application in a  
 1326 mineral province. *Geophysics*, 80(4), R175–R187.
- 1327 Tarantola, A. (2005). *Inverse problem theory and methods for model parameter esti-*  
 1328 *mation* (Vol. 89). siam.
- 1329 Ten Grotenhuis, S. M., Drury, M. R., Spiers, C. J., & Peach, C. J. (2005). Melt dis-  
 1330 tribution in olivine rocks based on electrical conductivity measurements. *Journal*  
 1331 *of Geophysical Research: Solid Earth*, 110(B12). doi: 10.1029/2004JB003462
- 1332 Tesauro, M., Kaban, M. K., & Aitken, A. R. (2020). Thermal and compositional  
 1333 anomalies of the Australian upper mantle from seismic and gravity data. *Geo-*  
 1334 *chemistry, Geophysics, Geosystems*, 21(11), e2020GC009305.
- 1335 Thiel, S., & Heinson, G. (2013). Electrical conductors in Archean mantle—result of  
 1336 plume interaction? *Geophysical Research Letters*, 40(12), 2947–2952.
- 1337 Trampert, J., Vacher, P., & Vlaar, N. (2001). Sensitivities of seismic velocities to  
 1338 temperature, pressure and composition in the lower mantle. *Physics of the Earth*  
 1339 *and Planetary Interiors*, 124(3-4), 255–267.
- 1340 Van Wijk, J., Baldridge, W., Van Hunen, J., Goes, S., Aster, R., Coblenz, D., ...  
 1341 Ni, J. (2010). Small-scale convection at the edge of the Colorado Plateau: Im-  
 1342 plications for topography, magmatism, and evolution of Proterozoic lithosphere.  
 1343 *Geology*, 38(7), 611–614.
- 1344 Wannamaker, P. E., Evans, R. L., Bedrosian, P. A., Unsworth, M. J., Maris, V.,  
 1345 & McGary, R. S. (2014). Segmentation of plate coupling, fate of subduction  
 1346 fluids, and modes of arc magmatism in Cascadia, inferred from magnetotelluric  
 1347 resistivity. *Geochemistry, Geophysics, Geosystems*, 15(11), 4230–4253.
- 1348 Wannamaker, P. E., Hasterok, D. P., Johnston, J. M., Stodt, J. A., Hall, D. B.,  
 1349 Sodergren, T. L., ... others (2008). Lithospheric dismemberment and magmatic  
 1350 processes of the Great Basin–Colorado Plateau transition, Utah, implied from  
 1351 magnetotellurics. *Geochemistry, Geophysics, Geosystems*, 9(5).
- 1352 Wellman, P., & McDougall, I. (1974). Cainozoic igneous activity in eastern Aus-  
 1353 tralia. *Tectonophysics*, 23(1-2), 49–65.



- 1354 Williams, C. K., & Rasmussen, C. E. (1996). Gaussian processes for regression. In  
 1355 *Advances in neural information processing systems* (pp. 514–520).
- 1356 Withers, A. C., Bureau, H., Raepsaet, C., & Hirschmann, M. M. (2012). Calibra-  
 1357 tion of infrared spectroscopy by elastic recoil detection analysis of h in synthetic  
 1358 olivine. *Chemical Geology*, *334*, 92–98.
- 1359 Xu, B., Griffin, W. L., Xiong, Q., Hou, Z.-Q., O’Reilly, S. Y., Guo, Z., . . . Zheng,  
 1360 Y.-C. (2017). Ultrapotassic rocks and xenoliths from South Tibet: Contrast-  
 1361 ing styles of interaction between lithospheric mantle and asthenosphere during  
 1362 continental collision. *Geology*, *45*(1), 51–54.
- 1363 Yaxley, G., Crawford, A., & Green, D. (1991, 11). Evidence for carbonatite  
 1364 metasomatism in spinel peridotite xenoliths from western Victoria, Aus-  
 1365 tralia. *Earth and Planetary Science Letters*, *107*, 305–317. Retrieved from  
 1366 <https://linkinghub.elsevier.com/retrieve/pii/0012821X9190078V> doi:  
 1367 10.1016/0012-821X(91)90078-V
- 1368 Yaxley, G., Green, D., & Kamenetsky, V. (1998, 11). Carbonatite metasoma-  
 1369 tism in the Southeastern Australian lithosphere. *Journal of Petrology*, *39*, 1917-  
 1370 1930. Retrieved from [http://dx.doi.org/10.1093/](http://dx.doi.org/10.1093/petroj/39.11-12.1917)  
 1371 [petroj/39.11-12.1917](http://dx.doi.org/10.1093/petroj/39.11-12.1917)
- 1372 Yoshino, T. (2010). Laboratory electrical conductivity measurement of mantle min-  
 1373 erals. *Surveys in Geophysics*, *31*(2), 163–206.
- 1374 Young, M., Cayley, R., McLean, M., Rawlinson, N., Arroucau, P., & Salmon, M.  
 1375 (2013). Crustal structure of the east gondwana margin in southeast australia  
 1376 revealed by transdimensional ambient seismic noise tomography. *Geophysical*  
 1377 *Research Letters*, *40*(16), 4266–4271.
- 1378 Yu, Y., Xu, X.-S., Griffin, W. L., O’Reilly, S. Y., & Xia, Q.-K. (2011). H<sub>2</sub>O contents  
 1379 and their modification in the Cenozoic subcontinental lithospheric mantle beneath  
 1380 the Cathaysia block, SE China. *Lithos*, *126*(3-4), 182–197.
- 1381 Zhang, M., & O’Reilly, S. Y. (1997). Multiple sources for basaltic rocks from Dubbo,  
 1382 eastern Australia: geochemical evidence for plume—lithospheric mantle interac-  
 1383 tion. *Chemical Geology*, *136*(1-2), 33–54.
- 1384 Zhang, M., Stephenson, P., O’REILLY, S. Y., McCULLOCH, M. T., & Norman,  
 1385 M. (2001). Petrogenesis and geodynamic implications of late Cenozoic basalts  
 1386 in North Queensland, Australia: trace-element and Sr–Nd–Pb isotope evidence.  
 1387 *Journal of Petrology*, *42*(4), 685–719.
- 1388 Zlotnik, S., Afonso, J. C., Díez, P., & Fernández, M. (2008). Small-scale gravi-  
 1389 tational instabilities under the oceans: Implications for the evolution of oceanic  
 1390 lithosphere and its expression in geophysical observables. *Philosophical magazine*,  
 1391 *88*(28-29), 3197–3217.